

1 Statistical Analysis of Contrail to Cirrus Evolution during the Contrail and Cirrus Experiments
2 (CONCERT)

3 Aurélien Chauvigné¹, Olivier Jourdan¹, Alfons Schwarzenboeck¹, Christophe Gourbeyre¹, Jean
4 François Gayet¹, Christiane Voigt^{2,3}, Hans Schlager², Stefan Kaufmann², Stephan Borrmann^{3,4},
5 Sergej Molleker^{3,4}, Andreas Minikin^{2,5}, Tina Jurkat², Ulrich Schumann²

6 ¹Laboratoire de Météorologie Physique, UMR 6016 CNRS/Université Clermont Auvergne,
7 Clermont-Ferrand, France.

8 ²Institut für Physik der Atmosphäre, Deutsches Zentrum für Luft- und Raumfahrt (DLR),
9 Oberpfaffenhofen, Germany.

10 ³Institut für Physik der Atmosphäre, Universität Mainz, Mainz, Germany.

11 ⁴Max-Planck-Institute for Chemistry, Department for Particle Chemistry, Mainz, Germany.

12 ⁵Now at: Flugexperimente, Deutsches Zentrum für Luft- und Raumfahrt (DLR), Oberpfaffenhofen,
13 Germany.

14 **Abstract:**

15 Air traffic affects cloudiness, and thus climate, by emitting exhaust gases and particles. The
16 study of the evolution of contrail properties is very challenging due to the complex interplay of
17 vortex dynamics and atmospheric environment (e.g. temperature, supersaturation). Despite
18 substantial progress in recent years, the optical, microphysical, and macrophysical properties of
19 contrails and ambient cirrus during contrail formation and subsequent ageing are still subject to
20 large uncertainties due to instrumental and observational limitations and the large number of
21 variables influencing the contrail life cycle. In this study, various contrail cases corresponding to
22 different aircraft types and atmospheric conditions are investigated using a statistical method based
23 on the in situ optical measurements performed during the CONCERT campaigns 2008 and 2011.
24 The two aircraft campaigns encompass more than 17 aircraft contrail cases. A Principal Component
25 Analysis (PCA) of the angular scattering coefficients measured by the Polar Nephelometer is
26 implemented. The goal is to classify the sampled ice cloud measurements in several clusters
27 representative of different contrail development stages (primary wake, young contrail, aged contrail,
28 and cirrus). Extinction and asymmetry coefficients, nitrogen oxide concentrations, relative humidity
29 with respect to ice and particle size distributions are analysed for each cluster to characterize the
30 evolution of ice-cloud properties during the contrail to cirrus evolution. The PCA demonstrates that
31 contrail optical properties are well suited to identify and discriminate the different contrail growth
32 stages and to characterize the evolution of contrail properties.

33 **1 Introduction**

34 Aircraft exhaust plumes have a significant impact on climate and tropospheric chemistry
35 (Lee et al., 2010; IPCC, 1999). The Intergovernmental Panel for Climate Change IPCC Special
36 Report on Aviation (1999) estimates that NO_x emissions from subsonic aircraft increase ozone
37 concentrations at cruise level. Short and long-lived pollution species have different impact on
38 atmospheric chemical composition depending on the flight level (Frömming et al, 2012). Emissions
39 of water vapour, black carbon (BC) / soot particles, sulphate (SO₄) aerosols and nitrogen oxides
40 (NO_x) contribute to the modification of the chemical composition of the upper troposphere on
41 shorter timescales (Lee et al., 2010, Gettelman and Chen, 2013; Liou et al., 2013). The long-term
42 climate impact is mainly driven by CO₂ emissions. Modelling studies have shown that the direct
43 radiative forcing from aviation is expected to represent 3-4% (50-60 mW m⁻²) of the anthropogenic

44 forcing (Lee et al., 2010; De Leon et al., 2012) and could reach 87 mW m^{-2} in 2025 (Chen and
45 Gettelman, 2016). Aircraft induced cloudiness has also an important impact on climate, although
46 the quantitative assessment of the radiative forcing remains a major source of uncertainties (Lee et
47 al., 2010).

48 1.1. Contrail formation and evolution

49 Contrail formation is mainly controlled by the thermodynamic properties of the ambient air
50 and by the aircraft emissions. The conditions for contrail formation can be determined by the
51 Schmidt-Appleman Criterion (SAC) (Schumann, 1996). Contrail chemical composition can have a
52 significant impact on the contrail formation (Kärcher et al., 2009). Indeed, contrail microphysical
53 properties such as the total number densities and ice crystal diameters are directly linked to the
54 emission index (e.g. soot emission index in kg-fuel^{-1}). Several studies in the past have been
55 dedicated to the evolution of concentrations of nitrogen oxide (NO) and sulphur dioxide (SO₂) and
56 their oxidized forms (Kärcher and Voigt, 2006 ; Voigt et al., 2006 ; Schäuble et al., 2009 ; Jurkat et
57 al., 2011).

58 Two different processes of contrail formation have been studied: combustion condensation
59 trails and aerodynamic condensation trails. Different studies (Gierens and Dilger, 2013; Jansen and
60 Heymsfield, 2015) have illustrated characteristics of aerodynamically controlled contrail formation
61 associated to warmer temperatures (observations at temperatures above -38°C). Contrails primarily
62 initiated by the combustion processes result from the mixing of hot and humid exhaust gases with
63 cooler and dryer ambient air. This increases the local relative humidity in the exhaust plume leading
64 to the formation of contrails when the saturation with respect to liquid water is reached. In this case,
65 soot and sulphate aerosols emitted by the aircraft (Moore et al., 2017) may act as condensation
66 nuclei to form liquid droplets. Homogeneous ice nucleation of the liquid droplets can occur when
67 the exhaust cools down through mixing with the ambient temperature, while preserving ice
68 saturation. Small ice crystals are then formed in the jet phase within some tenths of a second
69 (Kärcher and Yu, 2009).

70 The life-cycle of contrails depends on their interaction with the wake vortices behind aircraft
71 and the ambient atmosphere (Irvine et al., 2012; Graf et al., 2012; Duda et al., 2013; Carleton et al.,
72 2013; Schumann and Heymsfield, 2017). The ice crystals in the young contrails are captured within
73 two counter-rotating wake vortices in the downwash behind the aircraft induced by the aircraft lift,
74 which induce adiabatic compression, heating, and partial sublimation of the ice crystals within the
75 primary wake (Lewellen and Lewellen, 2001; Sussmann and Gierens, 2001, Unterstrasser et al.,
76 2008, Unterstrasser et al., 2016; Kärcher and Voigt, 2017). This primary wake may soon disappear
77 if ambient air is subsaturated with respect to ice. In the case of supersaturation, the secondary wake
78 becomes visible, thereby detraining ice particles from the primary wake at a higher level (Sussmann
79 and Gierens, 1999, Kaufmann et al., 2014). Quasi-spherical ice crystals become increasingly
80 aspherical and grow by uptake of water vapour as long as saturation with respect to ice is
81 prevailing. In ice-saturated conditions, contrails can persist after the vortex breakdown, spread and
82 evolve into contrail cirrus (Schumann and Heymsfield, 2017). The associated cloud cover (larger
83 than for linear contrails alone) increases the radiative forcing of contrail cirrus (Burkhardt and
84 Kärcher, 2011; Schumann et al., 2015).

85 1.2. Optical and microphysical properties of contrail phases

86 The assessment of the contrail radiative forcing requires, in particular, an accurate
87 estimation of the cloud cover, the visible optical depth, the single scattering characteristics, the ice
88 crystal effective size and habit (Yang et al., 2010; Spangenberg et al., 2013). Satellite observations

89 provide a comprehensive dataset to study statistically the contrail to cirrus evolution. The combined
90 contrail tracking algorithms on the Spinning Enhanced Visible and Infrared Imager (SEVIRI) on
91 board the Meteosat Second Generation (MSG) satellites with properties inferred by the Moderate
92 Imaging Spectroradiometer (MODIS) on board the Terra satellite was used by Vazquez-Navarro et
93 al., (2015) to characterize the properties of 2300 contrails. Properties included the lifetime (mean
94 values of 1 h), the length (130 km), the optical thickness (0.34), the altitude (11.7 km) and the
95 radiative forcing (-26 W m^{-2} for shortwave forcing over land) of these contrails.

96 However, detailed in situ optical and microphysical measurements are still needed to
97 evaluate satellite products and to develop more appropriate retrieval algorithm. Discriminating
98 contrails from natural cirrus from satellite observations remains extremely challenging. Although
99 the optical and microphysical properties of young contrails (linear contrails) differ from natural
100 cirrus properties, the contrail properties are highly time dependent, and persistent contrail cirrus can
101 be embedded in thin cirrus clouds. Recent in situ measurements (Voigt et al., 2017) show that the
102 microphysical properties of contrail cirrus can still be distinguished from natural cirrus at contrail
103 cirrus ages up to several hours.

104 Most of the previous studies (Jessberger et al., 2013; Lewellen et al., 2012 ; Schumann et al.,
105 2013) separate the contrail analysis between the two wakes phases. Primary and secondary wake
106 properties depend strongly on atmospheric conditions and aircraft type (emission index, vortex,
107 flight level, ambient humidity, temperature, ...). In the primary wake, contrail ice crystals are quasi-
108 spherical with values of the effective diameter (D_{eff}) typically lower than $4 \mu\text{m}$ (Schumann et al.,
109 2011; Gayet et al., 2012; Järvinen et al., 2016; Schumann et al., 2017b). The total number
110 concentration of ice particles is typically larger than 1000 cm^{-3} a few seconds after contrail
111 formation (Baumgardner and Gandrud, 1998; Petzold et al., 1997). Then, it decreases by dilution to
112 concentrations below 200 cm^{-3} within less than a minute after contrail generation (Poellot et al.,
113 1999; Schröder et al., 2000; Gayet et al., 2012). Gayet et al. (2012) reported mean values of ice
114 water content of 3 mg m^{-3} and maximum extinction coefficients close to 7 km^{-1} . In agreement with
115 these results, the recent overview on contrail studies presented in Schumann et al. (2017b) reports
116 several microphysical properties at different stages, for different atmospheric conditions as well as
117 comparisons with the Contrail Cirrus Prediction (CoCIP) model simulations. Their study highlights
118 the large variability (which increases with contrail age) of contrail properties.

119 Several studies reported findings on the secondary wake and its evolution into contrail
120 cirrus. Detained from the primary wake and submitted to saturated ambient air with respect to ice,
121 ice crystals grow rapidly, while crystal concentration decreases. Within the first minutes after
122 formation, measurements exhibit aspherical ice crystals with effective sizes up to $6 \mu\text{m}$, IWC
123 between 2.5 and 10 mg m^{-3} , extinction between 2 and 3 km^{-1} , and crystal concentrations typically
124 lower than 100 cm^{-3} (Goodman et al., 1998; Voigt et al., 2010; Kübbeler et al., 2011; Gayet et al.,
125 2012; Jeßberger et al., 2013; Schumann et al., 2013; Poellot et al., 1999; Febvre et al., 2009;
126 Kaufmann et al., 2014). Aged contrails can persist and evolve into contrail cirrus if the ambient air
127 is saturated with respect to ice. After a few minutes, tracking contrails by visual navigation is
128 challenging as contrail and contrail cirrus spread in the free troposphere. Aged contrails are often
129 difficult to identify unambiguously (Schumann et al., 2017a).

130 Observations of the ice crystal shape and their growth over several tens of minutes and up to
131 an hour illustrate that effective crystal sizes can easily exceed $20 \mu\text{m}$ with number concentrations
132 ranging from 1 to 5 cm^{-3} (Lawson et al., 1998; Schäuble et al., 2009), extinction less than 0.5 km^{-1}
133 (Febvre et al., 2009), and IWC up to 10 mg m^{-3} (Schröder et al., 2000; De Leon et al., 2012). At this
134 stage, within a sustained ice-supersaturated environment, contrail microphysical properties may still
135 differ from those of natural cirrus (Voigt et al., 2017) with concentrations of ice crystals larger than

136 100 μm in the order of 0.1 cm^{-3} . These crystals typically show bullet rosette type habits
137 (Heymsfield et al., 1998; Heymsfield et al., 2010). Optical depth values can reach values of 2.3
138 (Atlas and Wang, 2010), corresponding to an extinction of 0.023 km^{-1} . Nevertheless, the transition
139 from contrails to cirrus highly depends on the ambient saturation conditions. Modelling studies with
140 typical atmospheric conditions show a temporal evolution of the optical and microphysical
141 properties when contrails evolve to contrail cirrus clouds (Burkhardt and Kärcher, 2011;
142 Unterstrasser et al., 2016 ; Schumann et al., 2015).

143 In this study, we report on a powerful alternative to classify cloud events into young
144 contrails, aged contrails and cirrus. The method is applied to aircraft data of the CONCERT
145 (Contrail and Cirrus Experiment) campaigns (Voigt et al., 2010, 2011, 2014). The methodology
146 consists in implementing a Principal Component Analysis (PCA) of the angular light scattering data
147 measured by the Polar Nephelometer. The PCA patterns are classified to yield different cluster
148 representing specific contrail types. Corresponding optical, microphysical, and chemical properties
149 are derived for each contrail phase (from young contrails to contrail-cirrus). This paper starts with
150 an overview of the properties of contrails and cirrus clouds observed during two specific
151 CONCERT flights (19 November 2008 and 16 September 2011) encompassing a series of different
152 contrail evolution stages. These two flights contain a variety of contrail. The results from these
153 flights can be regarded as an analytical framework which then can be compared to contrails
154 properties of other flights.

155 **2 CONCERT projects and data processing**

156 2.1 CONCERT campaigns

157 The CONCERT-1 and CONCERT-2 campaigns took place in October/November 2008 and
158 August/September 2011, respectively. Both campaigns deployed the DLR Falcon 20 E research
159 aircraft from Oberpfaffenhofen, Germany, and sampled contrails and cirrus at mid-latitudes over
160 Europe. The overall objective was to reduce uncertainties on the microphysical, chemical, and
161 radiative properties of contrails behind aircraft of different types and to improve the evaluation of
162 contrail's impact on climate. A few CONCERT flights were also dedicated to study emissions of
163 Etna and Stromboli volcanos (Voigt et al., 2014; Shcherbakov et al., 2016). A few stratospheric
164 intrusions were also observed during the flight missions. In total, 23 flights were recorded during
165 the two measurement campaigns, wherein 12 flights were entirely focused on aircraft contrail
166 chasing. Overall, more than 17 different aircraft exhausts plumes have been probed. CONCERT-2
167 campaign mainly focused on the observation of persistent contrails, and hence on the evolution of
168 contrails to contrail cirrus.

169 During both CONCERT campaigns, the DLR research aircraft Falcon was equipped with a
170 set of instruments to measure the optical and microphysical properties of cloud particles and also
171 the trace gas composition in the UTLS (Upper Troposphere / Lower Stratosphere) region. Voigt et
172 al. (2010) provide a detailed description of the aircraft instrumentation. We briefly introduce the
173 instruments used in this study.

174 2.2 Aircraft instrumentation

175 The microphysical and optical particle properties of contrails and cirrus presented in this
176 study were mainly derived from the PMS Forward Scattering Spectrometer Probe 300 (FSSP-300),
177 the Polar Nephelometer (PN), and the PMS 2D-C hydrometeor imaging probe. The combination of
178 these independent techniques characterizes cloud particles within a range of diameters varying from
179 $0.5 \mu\text{m}$ to 2 mm .

180 The PN (Gayet et al., 1997) measures the angular scattering coefficients (non-normalized
 181 scattering phase function) of an ensemble of water droplets or ice crystals or a mixture of those
 182 particles ranging from a few micrometers to approximately 1 mm in diameter. These particles
 183 intersect a collimated laser beam, at a wavelength of 804 nm, near the focal point of a parabolic
 184 mirror. The light scattered at angles from 3.49° to 172.5° is reflected onto a circular array of 56
 185 near-uniformly positioned photodiodes. In this study, reliable measurements were performed at 30
 186 scattering angles ranging from ±15° to ±162°. Particle phase (water droplets and/or ice crystals) can
 187 be assessed as well as single scattering properties such as the extinction coefficient and the
 188 asymmetry coefficient with uncertainties of 25% and 4%, respectively (Gayet et al., 2002; Jourdan
 189 et al., 2010).

190 Particle size distributions and corresponding microphysical and optical integrated properties
 191 (IWC, Deff, N, and extinction) were derived from both FSSP-300 and 2DC measurements. The
 192 FSSP-300 (Baumgardner et al., 1992) measures the intensity of forward scattered light from cloud
 193 particles passing through the laser beam, with cloud particles in the diameter range 0.35-20 μm. In
 194 the forward angular region (from 4° to 12°), scattering is mainly described by the particle
 195 diffraction pattern and therefore depends on the refractive index, the shape, and the size of the
 196 particles. The method of data processing and size calibration used during the CONCERT campaigns
 197 have been presented in Gayet et al. (2012). We briefly recall that the asymmetry parameter derived
 198 from the PN was used to discriminate nearly spherical particles ($g \geq 0.85$) from non-spherical ones
 199 ($g < 0.85$) at 804 nm. For spherical ice particles, Mie calculations were used to derive the size bin
 200 limits and the corresponding extinction efficiency. Results were adjusted to the calibrated probe
 201 response. Additionally, to minimize Mie ambiguities related to the FSSP-300 size response, 31
 202 channels were rebinned to 13 channels with a diameter ranging from 0.5 μm to 18 μm (upper
 203 channels 30 and 31 were excluded from the data analysis). For non-spherical particles, the size of
 204 the contrail particles is expressed in terms of an equivalent surface or area diameter, i.e. the
 205 diameter of a sphere that has the same area than the projected area of the measured non- spherical
 206 particle image (Mishchenko et al., 1997; Schumann et al., 2011). The particles were assumed to be
 207 rotationally symmetric ice ellipsoids with an aspect ratio of 0.5. Accordingly, and contrary to the
 208 method used for spherical particles, 15 size bins ranging from 0.5 μm to 18 μm were defined based
 209 on T-Matrix calculations following Borrmann et al., (2000).

210 The bi-dimensional optical array spectrometer probe (2DC) provides information on the
 211 crystal size and shape within a nominal size range from 25 μm to 800 μm by recording cloud
 212 particles shadow images with a 25 μm resolution. The method of data processing used in this study
 213 is described in detail in Gayet et al. (2002) and Febvre et al. (2009). Reconstruction of truncated
 214 particles has been considered for the PSD calculations and the sampling surfaces have been derived
 215 according to Heymsfield and Parrish (1978). To improve the statistical significance of low particle
 216 concentrations, a 5-s running mean was applied. As the sensitivity of the probe to small particles
 217 decreases with airspeed (Lawson et al., 2006), particles smaller than 100 μm may not be detectable
 218 at the Falcon airspeed of typically 180 m s⁻¹. This may result in larger uncertainties of up to 100%
 219 in the derived microphysical parameters such as the IWC (Gayet et al., 2002 and 2004).

220 For spherical and non-spherical particles, the extinction coefficients are calculated from the
 221 following equation:

$$Ext = \frac{\pi}{4} \sum_i \beta_{ext}^i N_i D_i^2 \quad (1)$$

222 where β_{ext}^i is the extinction efficiency (values depend on spherical or aspherical particle
 223 characterization), D_i the mean diameter in channel i , and N_i the number concentration.

224 Different approaches are used to retrieve ice water content from spherical and non-spherical
 225 particles (Garret et al., 2003 ; Gayet et al., 2004 ; Gayet et al., 2012). For spherical particles (gPN >
 226 0.85), IWC is computed from the following equation:

$$IWC_{spherical} = \frac{\pi}{6} \rho_{ice} \sum_i N_i D_i^3 \quad (2)$$

227 with ρ_{ice} the bulk ice density (0.917 g cm⁻³).

228 For non-spherical ice crystals (gPN < 0.85 and for particle diameters larger than 50 μ m), an
 229 equivalent diameter method is used (Gayet et al., 2004). For an ice crystal with an area A, the
 230 particle equivalent diameter D_{equ} (in mm for eq. (3) and (4)), the equivalent mass x_{equ} (in mg), and
 231 the Ice Water Content (IWC in mg m⁻³) are defined as:

$$A \leq 0.049 \text{ mm}^2 \quad D_{equ} = 0.82A^{0.48} \quad (3)$$

$$A > 0.049 \text{ mm}^2 \quad D_{equ} = 0.56A^{0.32} \quad (4)$$

$$x_{equ} = \frac{\pi}{6} \rho_{water} D_{equ}^3 \quad (5)$$

$$IWC_{non-spherical} = \sum_i N_i x_{equ} \quad (6)$$

233 with ρ_{water} the bulk water density (1 g cm⁻³).

234 These equations do not account for possible shattering of large ice crystals on the probe
 235 inlets. This effect is minor in young contrails but can lead to an underestimation of large ice crystal
 236 concentration (diameters higher than 100 μ m) and thus an overestimation of small ice crystal
 237 concentration in contrail cirrus clouds (Febvre et al., 2009).

238 Trace gas measurements were also performed. NO/NO_y concentrations can be significant in
 239 young tropospheric aircraft plumes. NO and NO_y mixing ratio were performed using the
 240 chemiluminescence technique (Schlager et al., 1997) with a time resolution of 1 s. Instruments used
 241 for CONCERT campaigns are described in several studies (Jurkat et al., 2010 ; Jurkat et al., 2011 ;
 242 Voigt et al., 2014 ; Jurkat et al., 2016). The accuracy (and precision) of the NO and NO_y
 243 measurements are estimated with 7% (and 10%) and 10% (and 15%), respectively (Ziereis et al.,
 244 2000).

245 Relative humidity with respect to ice (RHI) is also key parameter to understand contrail
 246 formation and microphysical properties. Water vapour was measured with the chemical ionization
 247 mass spectrometer AIMS-H₂O during CONCERT-2 (Kaufmann et al., 2014; 2016). Hygrometers
 248 using the Lyman- α technique (FISH, Zöger et al., 1999; Meyer et al., 2015), and frost point
 249 hygrometers (CR-2, Heller et al., 2017) were deployed on the Falcon during CONCERT-1 and 2.

250 3 Results

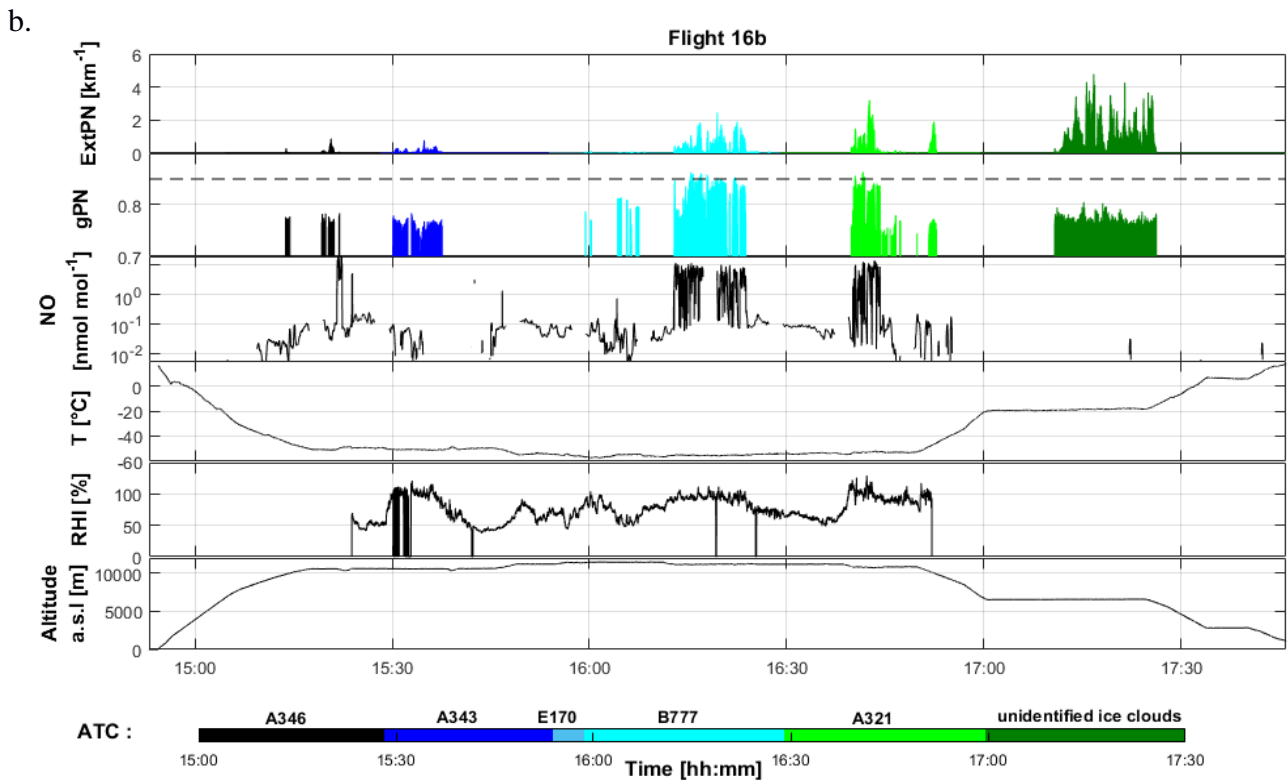
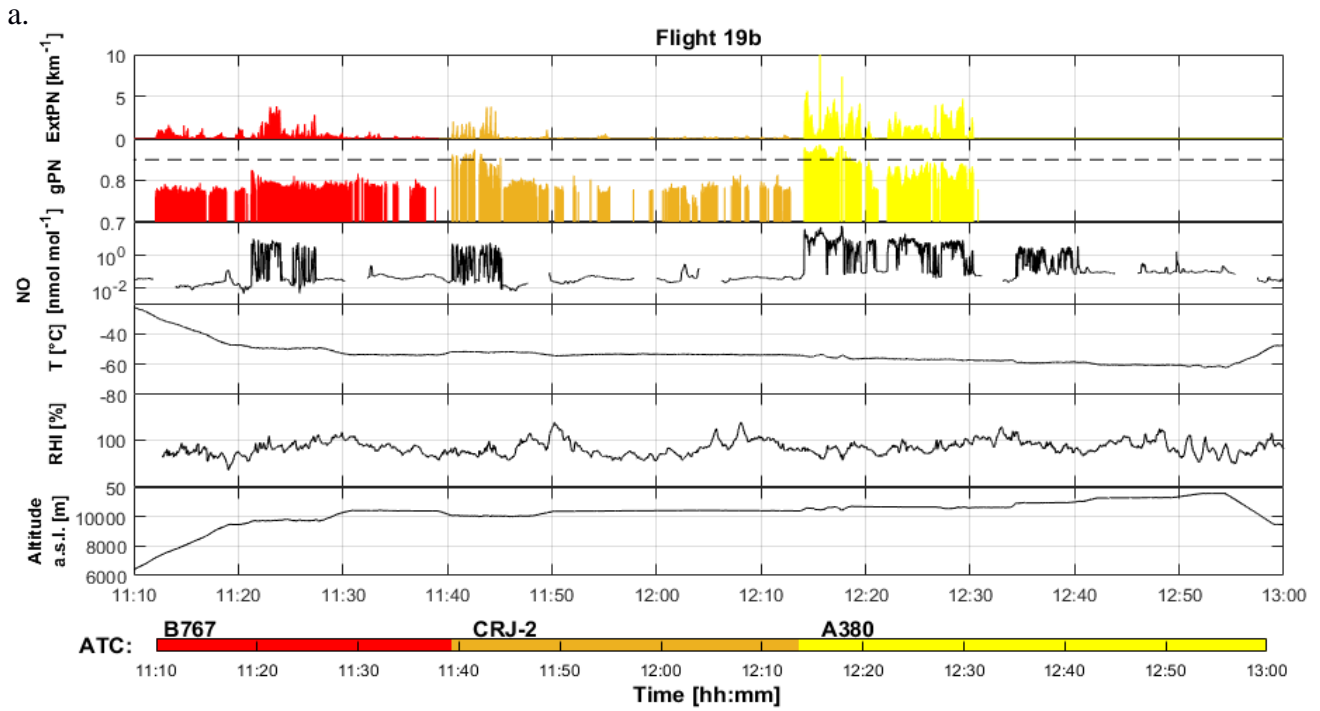


Figure 1: Time series at 1 s resolution for flights a) 19b (CONCERT 1) and b) 16b (CONCERT 2). From top to bottom: extinction coefficient (in km^{-1}) and asymmetry parameter measured by the Polar nephelometer at 804 nm (dashed line corresponds to a 0.85 value), concentration of nitric oxide (in nmol mol^{-1}) measured by chemiluminescence technique, temperature (in $^{\circ}\text{C}$), relative humidity with respect to ice (in %), and altitude a.s.l. (in m). Temporal series are coloured according to time and aircraft chasing information from Air Traffic Control (ATC).

252 The purpose of this section is to give an overview of the contrail optical properties and more
253 interestingly to evaluate the ability of the Polar Nephelometer measurements to identify contrails.
254 Two flights, performed on 16 September 2011 during CONCERT-2 (flight 16b) and on 19
255 November 2008 during CONCERT-1 (flight 19b), respectively, were selected for their variety of
256 ice clouds sampled during these two flights. The two flights are considered as a benchmark to
257 illustrate the potential of the PCA methodology described in Sect. 3.2.

258 Figure 1 displays the time series of the extinction coefficient (ExtPN) and the asymmetry
259 parameter (gPN) at a wavelength of 804 nm, relative humidity with respect to ice (RHI), the nitric
260 oxide (NO) concentration, the temperature T and the altitude for flights 19b and 16b. RHI measured
261 with the AIMS mass spectrometer is shown for both flights. For flight 19b, RHI instrument
262 shortcomings are discussed in details in Kübbeler et al. (2011), Gayet et al. (2012), Jessberger et al.
263 (2013) and Schumann et al. (2013). For both flights, Air Traffic Control (ATC) provides
264 information on the flight tracks and on the chased aircraft (aircraft type, engine type, fuel flow,
265 weight, engine power setting). From this information, the Falcon measurements were attributed to
266 the exhaust plume of individual aircraft with an estimated plume age. Time series are colour coded
267 according to ATC information. When no ATC information is available, the cloud segment is called
268 “unidentified ice cloud”.

269 The PN extinction coefficient coupled with the asymmetry parameter seems to be a
270 reasonable proxy to detect contrails and cirrus clouds (see amongst other references, Voigt et al.,
271 2010). ExtPN values, by definition, depend on the cloud particle concentration and size. Values
272 typically beyond 0.1 km^{-1} correspond to cloud events that are well correlated to environmental
273 conditions supersaturated with respect to ice ($\text{RHI} > 100\%$). Figure 1 shows that relatively high
274 values of extinction can be found in flights 19b and 16b that are linked to the presence of contrails
275 or ice clouds. Moreover, the temporal distributions of these values are in accordance with ATC
276 information for both flights. For instance, most of the contrails induced by commercial aircraft
277 exhaust plumes are associated with significant extinction coefficient values. The ExtPN values are
278 between 0.2 km^{-1} and 10 km^{-1} for contrails induced by A346, A340, and A380 commercial aircraft.

279 The last cloud event (“unidentified ice cloud”) during flight 16b is not a contrail because it
280 is measured at temperatures significantly above the Schmidt Appleman temperature (-38°C ,
281 Schumann 1996). This is an ice cloud with high extinction ($> 0.5 \text{ km}^{-1}$) and low asymmetry values
282 (< 0.75), characteristic for ice particles (Jourdan et al., 2003b, Febvre et al., 2009). Relative
283 humidity and NO mixing ratio data are not available for this cloud.

284 Most of the aircraft induced contrails are detected by the PN except for the ones stemming
285 from the E170 airplane. At 15:50 during flight 16b, ATC identified the E170 position close to the
286 Falcon flight trajectory, however the ExtPN and the NO mixing ratio remained low. Hence, the
287 E170 contrail was not probed by the Falcon. In the following we assume that only periods with
288 ExtPN values above 0.1 km^{-1} are considered as a reliable signature of contrails.

289 The absolute values of the asymmetry parameter gPN provide additional information on the
290 cloud particle shape. Indeed, gPN is a good indicator of the degree of sphericity of ice crystals
291 (Gayet et al., 2012). Ice clouds with gPN values higher or equal to 0.85 are typically composed of
292 spherical ice crystals, whereas lower values are indicative of aspherical ice particles. In a
293 supersaturated environment, crystals grow by water vapour deposition and become increasingly
294 aspherical with time. However, in very young contrails, spherical ice crystals with an asymmetry
295 coefficient around 0.85 prevail. gPN is decreasing when water vapour diffusion is generating more
296 and more aspherical crystal shapes at ice supersaturation. This can be observed for A321 chasing
297 during flight 16b where gPN is decreasing to a value of 0.75 whilst RHI remains around 100%. This

298 is not the case during B777 chasing where no gPN decrease is observed when RHI < 100%.
299 However, it is important to note that the RHI measurements during the CRJ-2 chasing events do not
300 show supersaturated conditions, whereas contrail seems persistent. Indeed, RHI measurements
301 should be discussed carefully for this campaign due to potential calibration issues.

302 A good example of the evolution of gPN is the CRJ-2 contrail observed between 11:40 and
303 11:45 during flight 19b. The sequence illustrates the potential of the gPN measurement to
304 characterize the evolution of contrail properties. The evolution of the ice crystal shape is reflected in
305 the decrease of the asymmetry parameter from 0.88 to 0.79 (uncertainties around 0.04) after only 5
306 min and down to 0.77 after 20 min. A weaker decrease of gPN values (around 0.78 ± 0.02) is then
307 observed until 12:10 corresponding to 30 min of contrail ageing. During this period, ice crystals are
308 expected to grow by water vapour diffusion. A similar decrease of gPN values has been reported by
309 Gayet et al. (2012) in the ageing contrail from an A380 aircraft, and is also visible in the present
310 study for the B767 and the A321 contrails.

311 NO concentration measurements can also be used to discriminate natural cirrus clouds from
312 clouds influenced by aircraft traffic. At the typical altitude of 10 km, NO environmental
313 concentrations are close to background values. In contrast, NO concentrations in young contrails
314 may reach several tens of nmol mol^{-1} (Voigt et al., 2010). Figure 1 shows a good correlation
315 between the expected localization of young contrails and NO concentrations. The dilution effect in
316 the upper troposphere causes an important decay of chemical concentrations. For instance, the first
317 few seconds of the A380 chasing during flight 19b are characterized by a high NO concentration
318 (up to 40 nmol mol^{-1}) followed by a fast decrease to 10 nmol mol^{-1} in the next 15 min of
319 observation time, and less than 5 nmol mol^{-1} later. NO concentrations finally decrease to
320 background levels within hours (e.g. Voigt et al., 2017). This decrease of the NO concentration is in
321 accordance with the decrease of the extinction coefficient (from 10 to 0.2 km^{-1}) and asymmetry
322 parameter (from 0.88 to 0.77). NO is mainly used as an additional contrail indicator. However,
323 during some aircraft chasing events, NO concentrations were near background levels, while mass
324 spectrometric measurements (not shown here) indicate elevated concentrations of HONO, HNO_3 ,
325 and SO_2 representative for contrail chemical species.

326 Flights 19b and 16b clearly show that the optical properties can be used to discriminate
327 different cloud events. A first order analysis of these parameters (supported by the ATC
328 information) can be used to roughly distinguish young contrails (mostly quasi-spherical ice crystals)
329 from aged contrails (mostly aspherical ice crystals). This analysis is mainly qualitative and based
330 solely on a few typical parameters (Fig. 1). A more robust statistical method should be used to
331 accurately separate the different contrail phases. In the following section, scattering properties are
332 investigated more extensively to assess whether the information content of the PN scattering
333 measurements is sufficient to document changes in the contrail microphysical properties.

334 3.2 Statistical Method

335 In this section, we present a methodology based on a statistical analysis of the optical
336 signature of the cloud measurements. The goal is to classify the contrail properties according to the
337 aircraft origin and evolution stage. The main objective of the Principal Component Analysis (PCA)
338 is data reduction to allow a better physical interpretation of the light scattering patterns derived
339 from the Polar Nephelometer measurements (Legendre and Legendre, 1998; Jourdan et al., 2003).
340 In this study, optical properties of ice crystals in the evolving contrail environment are examined to
341 evaluate contrail evolution. This statistical analysis was already successfully applied to discriminate
342 mixed phase clouds (Jourdan et al., 2003; Jourdan et al., 2010) from liquid clouds and ice clouds,
343 and to identify porous aerosol in degassing plumes (Shcherbakov et al., 2016).

344

3.2.1 Reference definition

345 The PCA is first applied to the PN angular scattering coefficients measurements performed
 346 during flights 16b and 19b which are here considered as our reference dataset. Initially, a
 347 correlation matrix is calculated to characterize the link between each scattering angle. The PCA is
 348 designed to generate a new limited set of uncorrelated parameters, called principal components C_{lj}
 349 representative of the original data set variability.

350 A first implementation of the PCA is performed to detect unreliable data or out of order
 351 photodiodes. For instance, seven photodiodes presented a low signal to noise ratio and were
 352 excluded from the dataset. Flight sequences characterized by $\text{ExtPN} < 0.1$ were also removed.
 353 Finally, flight sequences dedicated to aircraft chasing and ice cloud sampling were considered to
 354 perform a second PCA. The analysis is performed on the remaining angular scattering coefficients
 355 (4669 Angular Scattering Coefficients (ASC) representing PN measurements of flights 16b and
 356 19b) restricted to 25 angles θ ranging from 15° to 155° . The new set of variables or coordinates,
 357 C_{lj} , can be expressed with the scalar product of the vector of reduced angular scattering coefficients
 358 $\overline{\sigma}_j(\theta)$ for the j^{th} measurements, expressed in log scale, and the l^{th} eigenvector $\xi_l(\theta)$ (i.e. principal
 359 component) of the total data set correlation matrix (Jourdan et al., 2010).

$$C_{lj} = (\overline{\ln\sigma_j} - \langle \overline{\ln\sigma} \rangle)^T \cdot \xi_l \quad (4)$$

360 where $\langle \overline{\ln\sigma} \rangle$ represents the average ASC of the dataset.

361 The first three eigenvectors $\xi_l(\theta)$ of the correlation matrix are displayed in Fig. 2 along with
 362 their normalized eigenvalues λ_l , representing more than 99% of the variability of the PN angular
 363 scattering coefficients (ASC).

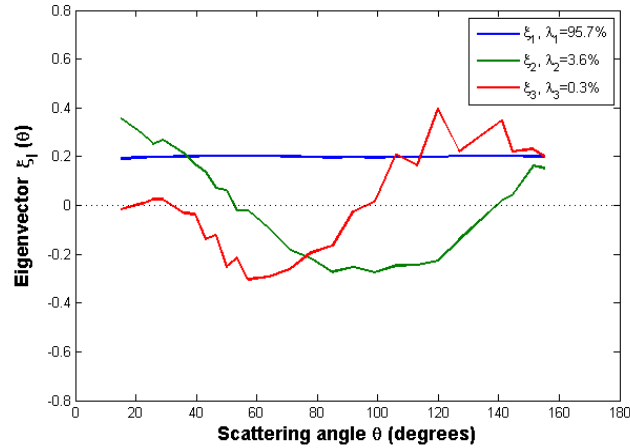


Figure 2: First three eigenvectors for the flights 16b and 19b.

364 The first eigenvector $\xi_1(\theta)$ is approximately constant versus scattering angle and represents
 365 95.7% of the total variance. It means that this principal component is representative of changes of
 366 the magnitude of phase functions without any changes in their global shape. This behaviour means
 367 that 95.7% of the ASC variations are linked to changes of the cloud particle extinction. Results
 368 show a good correlation ($r^2 = 0.98$) between the first eigenvector and the extinction derived from the
 369 PN measurements (ExtPN).

370 The second eigenvector $\xi_2(\theta)$ reverses sign twice at scattering angles equal to 50° and 140°
371 with an extremum around 90° . Accordingly, 3.6% of the angular scattering variability corresponds
372 to a redistribution of scattered energy from the angular region (50° - 140°) to scattering angles lower
373 than 50° and higher than 140° . Light-scattering modelling studies demonstrate that the scattering
374 behaviour in the angular region between 60° and 140° is sensitive to the particle shape and
375 thermodynamic phase (Jourdan et al., 2010). A strong linear correlation ($r^2=0.97$) between the
376 second eigenvector and the asymmetry coefficient (gPN) at 804 nm is found.

377 The third eigenvector represents only 0.3% of the total variance. However, this eigenvector
378 provides additional information in scattering regions which are not well described by the first two
379 principal components. It has opposite signs in the angular region (30° - 90°) and (90° - 155°) with
380 maximum extremal values at 60° and 120° . The shape of the third eigenvector describes the
381 forward/backward hemisphere partitioning of the scattering. Baran et al. (2012), Xie et al. (2006),
382 and Xie et al. (2009) showed that the scatter pattern for angles between 120° and 160° ,
383 corresponding to ice bow-like effects, is sensitive to quasi-spherical particles. Moreover, these
384 backscattering angles ($\theta > 120^\circ$) and scattering angles around 22° and 46° (corresponding to halo
385 features) can also be linked to the particle habits and surface roughness (Xie et al., 2009, Jourdan et
386 al., 2010).

387 Each phase function (or ASC) measured by the PN can be expressed with a good accuracy
388 as a linear combination of the three principal components (Jourdan et al., 2010). The PN data are
389 projected into a new space defined by the three principal components (3D-space) instead of the 25-
390 dimensional space of ASC. The scatterplots of the C_{j3} and C_{j1} expansion coefficients versus the C_{j2}
391 coefficient are represented on Fig. 3a and b respectively. Fig. 3a illustrates the features of the ASC
392 measurements in one of the most comprehensive way. Each point corresponds to a measured phase
393 function documented over 25 angles. The variability of C_{j2} coefficients is significant with values
394 ranging from -1 to 1.5. The angular variation of the second principal component indicates that large
395 values of C_{j2} ($C_{j2} > 0.75$) correspond to ASC with low side scattering (60° - 130°) and higher forward
396 scattering (15° - 40°) and somehow higher backscattering (145° - 155°). This behaviour is connected to
397 an increase of the asymmetry parameter with an increase of C_{j2} values. Thus, the fraction of
398 spherical particles increases with increasing C_{j2} . In the region defined by negative values of C_{j2} the
399 density of points is relatively high. These cloud events exhibit optical properties characterized by a
400 large side scattering and low asymmetry parameter. Therefore, specific cloud sequences sharing
401 similar scattering properties can be identified based on this second principal component. Young
402 contrails characterized by quasi-spherical ice crystals have high positive values of C_{j2} while cirrus
403 clouds and contrail cirrus exhibit high negative values.

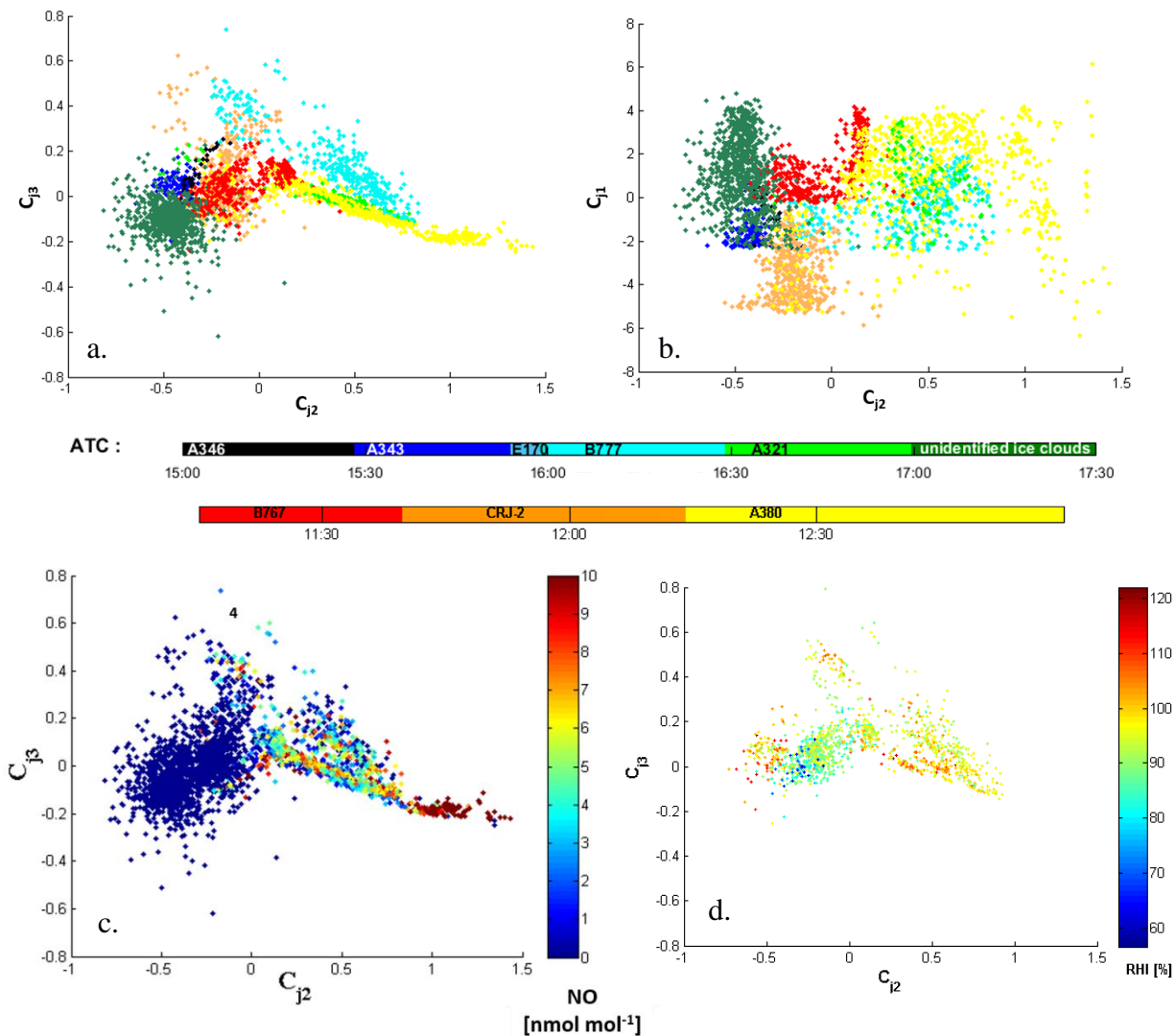


Figure 3: Expansion coefficient diagram for flights 16b and 19b: third versus second principal component for a), c) and d), and first versus second principal component for b). Data points are colour coded according to ATC information for a) and b), by NO concentration for c), and by RHI values for d).

404 In the space of the third principal component high positive values of C_{j3} imply that less
 405 energy is scattering in the forward hemisphere and thus more energy is scattered in the backward
 406 hemisphere. The variability of the expansion coefficients is less pronounced as ASC are distributed
 407 between -0.4 and 0.6. Most of the measured ASC do not significantly differ from the average ASC
 408 in the angular ranges (30° - 90°) and (90° - 155°). However, some specific clusters linked to scattering
 409 behaviour can be identified for values of C_{j3} greater than 0.1 and lower than -0.1. These threshold
 410 values also depend of the position of the ASC on the second principal component. Finally, the first
 411 principal component is directly linked to the extinction coefficient. High values of C_{j1} are
 412 representative of optically dense cloud sequences.

413 Figure 3c shows an increase of C_{j2} for increasing NO mixing ratio. This clearly indicates
 414 that the contrails are evolving in space and/or time along the Falcon flight track. Hence, contrails
 415 characterized by a low side scattering due to the presence of spherical ice crystals correspond to
 416 high NO concentration. This behaviour can be a signature of young contrail properties. Elder or
 417 aged contrails composed of a higher fraction of non-spherical crystals or growing more aspherically
 418 are expected to exhibit an enhanced side scattering and a lower asymmetry parameter associated to

419 lower NO concentrations. RHI measurements also give relevant information on the capacity of the
 420 cloud to be persistent. Thus, Fig. 3d shows higher RHI values with decreasing gPN values.

421 3.2.2 Clustering analyses

422 The new representation of each measurement in the space of the first three principal
 423 component reveals different clusters, characteristic of specific scattering behaviour. The clustering
 424 k-mean method (Seber 1984, Spath 1985) is applied to the reference dataset (flights 19b and 16b) to
 425 partition the observations into k clusters to minimize the variance within each cluster (i.e. to
 426 minimize the distance between each data point and the centre of the cluster it belongs to). The
 427 number of cluster k is an adjustable parameter. Then in a first step, each observation is assigned to a
 428 specific cluster whose mean has the least squared Euclidean distance (i.e. nearest mean). In a
 429 second step, the position of each cluster is set to the mean of all data points belonging to that cluster
 430 (i.e. the centroids of each of the k clusters becomes the new means). These two steps are repeated
 431 until convergence is reached when the assignments no longer change.

432 Sixteen clusters were found to encompass all points of the two flights and to partition each
 433 aircraft chasing identified from ATC information (Fig. 3a and 3b). For clarity and better
 434 understanding of the variability of contrail properties, we choose to limit the number of clusters to
 435 6. 9 of the original clusters are merged into 2 clusters (clusters 3 and 5) presenting similar NO
 436 concentrations and optical properties. Four of the original clusters are combined into one new
 437 cluster containing the A321 / A380 contrails (referred to as Cluster 2 hereafter). In addition, only
 438 data points within the 10% of the maximum Mahalanobis distance (De Maesschalck et al., 2000) to
 439 the respective cluster's centre are kept for further analysis.

440 Clusters are defined by their means (or centres), standard deviations (or widths), and cross-
 441 correlations (or tilts). The Mahalanobis distance is given by the equation:

$$D_M(x)_i = \sqrt{(x - \mu_i)^T S_i^{-1} (x - \mu_i)} \quad (5)$$

442 with D_M the Mahalanobis distance between point χ and the i^{th} cluster center, μ_i the N-dimensional
 443 mean of this cluster and S_i its covariance matrix.

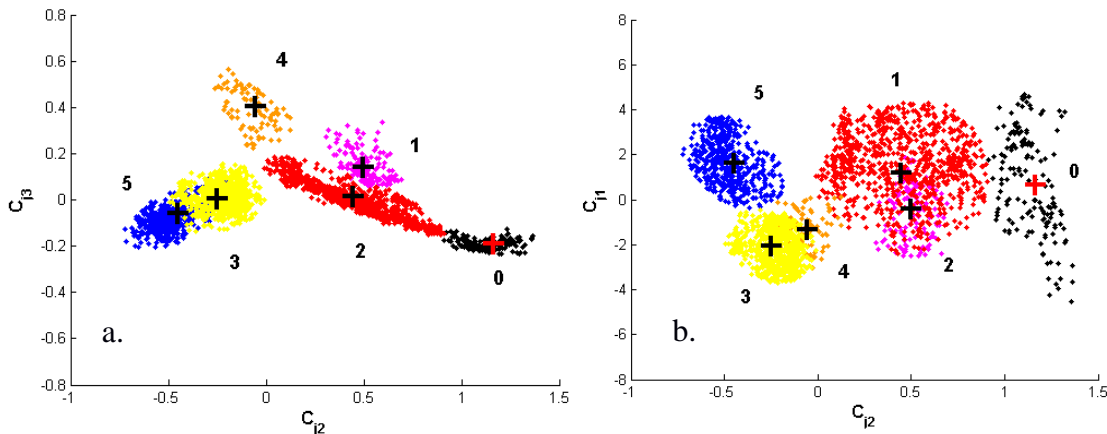


Figure 4: Clustering results of the k-mean method applied to the base (flights 16b and 19b). Third versus second principal component for a), and first versus second principal component for b). Only data within the 10% of the maximum Mahalanobis distance to the respective cluster's centers have been considered for this analyse.

444 Figure 4 shows the partitioning of the dataset into the 6 new clusters (clusters 0 to 5). In the
 445 following we use data from chemical tracers and optical measurements, and aircraft type
 446 information to support and discuss the results of the k-means clustering method.

447 Clusters 3 and 5 are characterized by very low NO concentrations (Fig. 3c). These cloud
 448 events have similar optical properties, in particular a low asymmetry parameter, high side scattering
 449 behaviour, and often supersaturated ambient conditions with respect to ice. According to ATC
 450 information, these clusters both contain parts of the measurements in the B767, A343, A346 and
 451 CRJ-2 contrails. In addition, the unidentified ice cloud event from flight 16b is fully included in
 452 cluster 5. Unpolluted natural cirrus was rarely observed during the CONCERT campaigns (Voigt et
 453 al., 2010). Since we have no objective way of discriminating natural cirrus from contrail cirrus
 454 region, these clouds are referred to polluted cirrus or PC, and cluster 3 to aged contrails.

455 Clusters 0, 1, 2, and 4 correspond to higher NO concentrations representative of a
 456 significant aircraft exhaust influence. Contrail data for the A380 aircraft are included in clusters 0
 457 and 2 while the ones corresponding to the B777 are assigned to clusters 1 and 4. Pictures from an
 458 onboard camera reveal that the data in cluster 0 come mainly from the contrail in the primary wake
 459 of the A380.

460 The contrail and cirrus classification based on ASC measurements appears to be consistent
 461 with the independent trace gas measurements. Each cluster represented on Fig. 4 can be linked to a
 462 distinct cloud event. Therefore, the combination of flights 16b and 19b can provide a relevant test-
 463 bed database to discriminate contrail properties. Young contrails (spherical ice crystals) are
 464 associated to clusters 0, 1 or 2, whereas aged contrails (aspherical ice crystals and high RHI values)
 465 with more pristine ice are categorized in clusters 3 and 4. Table 1 summarizes the cluster definitions
 466 and names used in this work.

467

Cluster number	definition	name
0	Primary Wake	PW
1	Young Contrail 1	YC1
2	Young Contrail 2	YC2
3	Aged Contrail 1	AC1
4	Aged Contrail 2	AC2
5	Polluted Cirrus	PC

Table 1: Cluster's definitions according to ATC information and tracer measurements (NO concentrations and RHI values)

468 One should keep in mind that some points are still attributed to a particular cluster without
 469 strong physical justification.

470 3.2.3 Merging other CONCERT flights

471 In this section, we complement the previous analysis with additional cloud optical
 472 measurements performed during other CONCERT flights to increase the robustness of the method.

473 The ASC measured during other flights can be projected in the space of the principal
 474 components established with flights 16b and 19b dataset. The coordinates of the data points
 475 corresponding to the other flights are calculated from Eq. (4). An example of this data projection is
 476 illustrated in Fig. 5 where flight 17a is represented in the C_{j2}/C_{j3} space. Each data point can be
 477 attributed to one cluster previously defined by the k-mean clustering method based on flights 16b
 478 and 19b dataset (black points). In other words, the ASC measured during another flight can be
 479 merged (projected) into the expansion coefficient diagram displayed on Fig. 3. Data points sharing
 480 similar optical properties will be close to each other on such plot. Figure 5 shows that different
 481 contrail phases are observed during flight 17a. Data points are mostly grouped into cluster AC1, but
 482 are also present in clusters AC2, YC2, and PW. Finally, cloud data gathered during this flight are
 483 mainly categorized as young and aged contrails. We follow this methodology to project and classify
 484 each additional contrail event performed during both CONCERT campaigns with minimum
 485 Mahalanobis distance (see Eq. (5)).

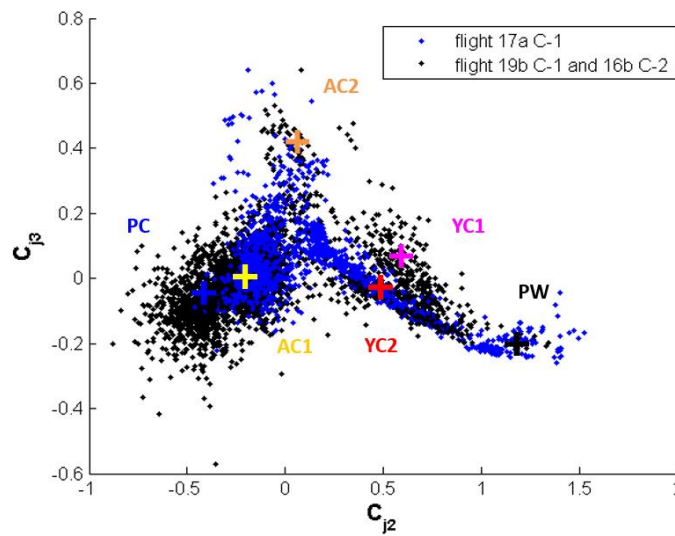


Figure 5: Example of data projection in the C_{j2}/C_{j3} space where data from flight 17a (blue data points) are superposed on the data from the benchmark flights 19b and 16b (black data points).

486 The assignment of the data points to the six clusters shown on the expansion diagrams is
 487 summarized in Table 2. Eight flights (6 additional flights) representing 4426 ASC measurements
 488 were processed. The lengths of the bars in Table 2 represent the distribution of the data points
 489 within the different clusters: a) black bars correspond to the fraction of cloud events within a
 490 specific flight (with extinction coefficient higher than 0.1 km^{-1}) and b) blue bars represent cases of
 491 individual contrails within the flight. Data points with extinction coefficient lower than 0.1 km^{-1}
 492 are not shown in the table. More than 30% of the data points are located in clusters AC1 and/or PC
 493 meaning that they correspond to aged contrail and sometimes polluted cirrus. Flights clearly
 494 performed in well visible contrails outside cirrus (earlier development stage and/or intensified
 495 persistent elder contrails) exhibit significant fraction of data points associated to clusters PW, YC1,
 496 and YC2 (young contrails) for both CONCERT-1 and CONCERT-2 campaigns. However, within
 497 these flights data points are also gathered in cluster AC1 (aged contrails) and to a lesser extent in
 498 cluster AC2 (mostly corresponding to measurements performed during two different B777 contrail
 499 chasing events).

500 These results are in reasonable agreement with previous conclusions (this subsection) drawn
 501 for the cluster definitions and associated contrail / ice cloud characteristics. Very young contrails
 502 have been mostly chased during CONCERT-1 (flights 19a and 19b). Another interesting result is

503 related to flight 17 during CONCERT-2 (flight 17 C-2) where no aircraft information was provided
 504 by ATC. Still ATC data indicate measurements in exhaust plumes and the Falcon flew apparently in
 505 visible contrails (ExtPN > 0.1 km⁻¹) which were probably too old for ATC recognition. Our analysis
 506 shows that these data points can mainly be attributed to cluster PC and AC1. This observation
 507 suggests that significantly aged contrails have been sampled. However, crystal formation and
 508 growth processes in contrails and polluted cirrus suggest that very old contrails more and more
 509 resemble natural cirrus properties.

Day / Aircraft		Cluster						Number of points	Age (s)
		PW	YC1	YC2	AC1	AC2	PC		
		1st wake	young contrails		aged contrails		Polluted Cirrus		
17a C-1	TOTAL							1435	
	A340-311							359	61 - 144
17b C-1	TOTAL							2715	
	B737-500							310	77 - 151
	A340-642							100	82 - 139
	NC							189	-
19a C-1	TOTAL							2152	
	A319-111							628	94 - 129
	A340-311							175	63 - 90
19b C-1	TOTAL							1647	
	B767-300							319	77 - 107
	CRJ-2							151	80 - 95
	A380-841							677	109 - 240
20 C-1	TOTAL							1434	
	B737-300							64	90 - 290
16b C-2	TOTAL							1511	
	A340-600							128	100 - 132
	B777							378	120 - 160
17 C-2	TOTAL							135	70 - 95
	NC1							498	-
	NC2							233	-
24 C-2	TOTAL							1380	
	B777							371	112 - 178

Table 2: Classification relative to the six clusters on the Cj2/Cj3 representation of the PCA of all data points for each flight of the two CONCERT campaigns (C-1 in November 2008 and C-2 in September 2011). The legend of the bars represents the relative contribution of data points of individual contrails (blue bars) and also entire flights (black bars) to the 6 individual clusters.

510 ATC information on exhaust plume ages was also collected during each chasing. Some
 511 chasings were performed less than 100 s after contrail formation. This is the case for the A340
 512 contrail during flight 19a and for the CRJ-2 contrail during flight 19b of CONCERT-1 and for the
 513 A321 contrail during flight 16b of CONCERT-2. One can notice that the contrail ages are well
 514 correlated to the chosen cluster definitions, revealing that contrail data relative to the A340 are
 515 included in cluster PW and YC2 (young contrails) for more than 90% of the data points, and nearly
 516 63% for the CRJ-2 and 84% for the A321. According to our cluster classification, only 5% of the
 517 data points gathered during these three flights correspond to aged contrail (cluster AC1 and AC2)
 518 categories in contrast to other CONCERT-1 and CONCERT-2 flights (with more than 30% of data
 519 points associated to AC1 and AC2). Even though it is still difficult to associate contrail ages to
 520 measurement points, the “contrail age” ranges agree with the cluster definitions.

521 4 Evolution of contrail properties

522 4.1 Optical and chemical cluster properties

523 In the previous section, we showed that cloud events can be separated according to their
524 light-scattering properties. Six clusters were defined based on two flights having a significant
525 number of data points distributed in each cluster. In this section, we present the mean optical,
526 chemical, and microphysical properties for each cluster. The average properties are calculated for
527 all data points associated to the 6 individual clusters (all flights, both CONCERT campaigns).
528 Figures 6a, 6c, and 6d show the normalized frequency distributions of the asymmetry parameter
529 (gPN), the extinction coefficient (ExtPN), and NO concentrations for the six clusters, respectively.
530 Figure 6b represents the mean normalized scattering phase functions of each clusters. However, it
531 should be noted that the number of data points could differ significantly from one cluster to another
532 (from 141 measurements for Cluster YC1 to 8950 measurements for Cluster AC1).

533 The asymmetry parameter gPN statistics shown in Fig. 6a provides the most striking
534 evidence of the relationship between contrail evolution stage and optical properties. In agreement
535 with findings of Gayet et al. (2012), aged contrails (cluster AC1 and AC2) and polluted cirrus
536 (cluster PC) correspond to gPN values ranging from 0.72 to 0.80. Younger contrails (cluster YC1
537 and YC2) have values of gPN of 0.80 to 0.86. Values of the asymmetry parameter in the primary
538 wake (cluster PW) are typically above 0.86. These features are a consequence of the time evolution
539 of ice crystal shapes from quasi-spherical ice particle after exhaust to non-spherical (e.g. column,
540 needle, bullet, and bullet-rosette type crystals) as the contrail evolves. In the primary wake, the
541 pressure increases in the descending vortex. This leads to adiabatic heating and subsequent
542 sublimation of the ice crystals (Lewellen and Lewellen, 2001; Unterstrasser et al., 2016) that can
543 explain the spherical shapes of ice crystals and thus, the high values of the asymmetry coefficients.

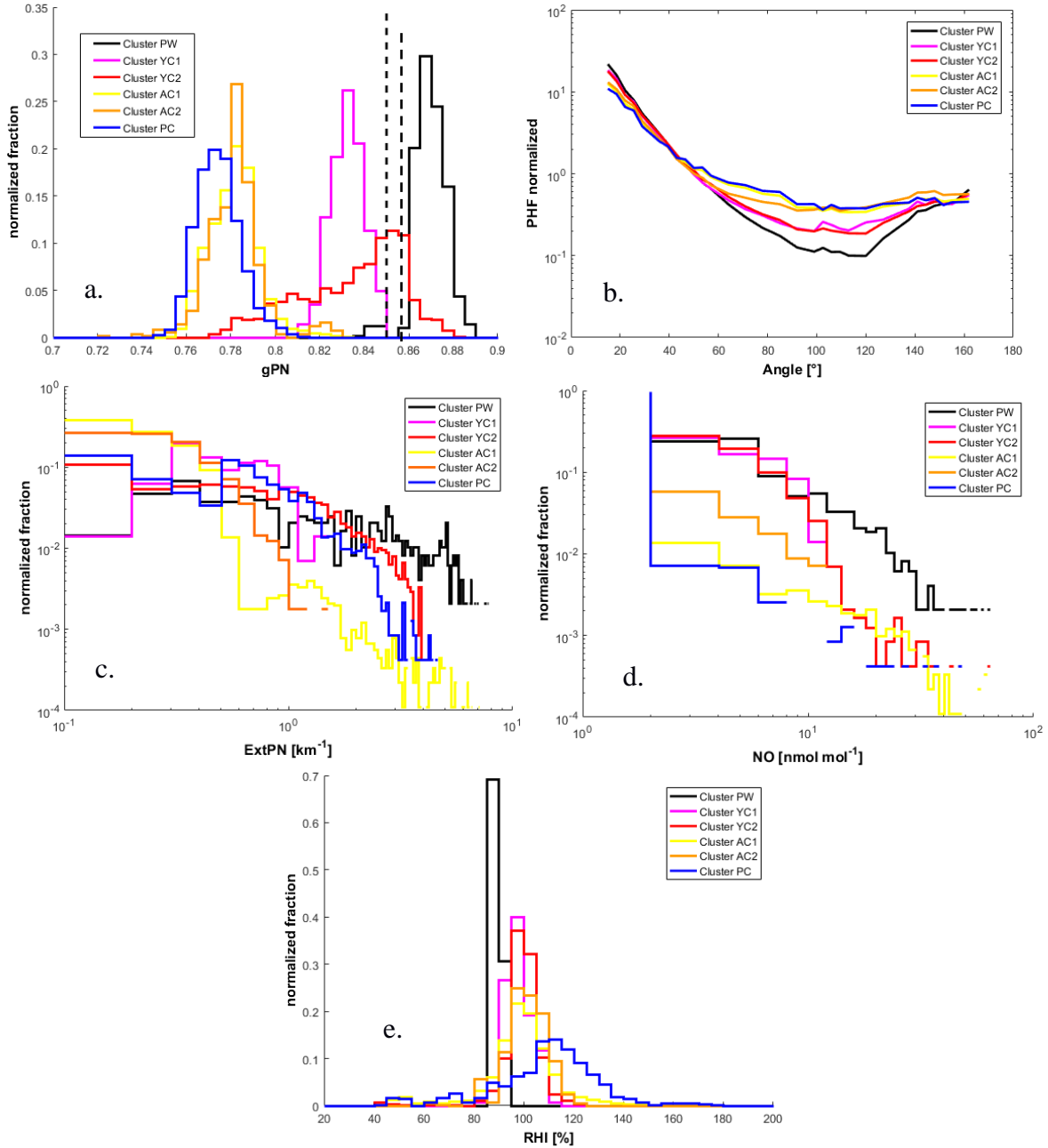


Figure 6: Normalized histograms of a) asymmetry coefficient (dashed line corresponds to a value of 0.85), b) phase function, c) extinction retrieved by Polar Nephelometer, d) NO concentration for all flights, and e) RHI conditions for CONCERT-2 flights.

544 Figure 6b shows the normalized phase functions. Primary wake phase functions (cluster
 545 PW) are clearly different from the young contrail phase functions (cluster YC1 and YC2), which are
 546 themselves different from aged contrails (cluster AC1 and AC2) and polluted cirrus (cluster PC)
 547 phase functions. The main difference can be seen in the side scattering region (50°-140°). This
 548 region is sensitive to the ice particles shapes and to the fraction of spherical ice crystals within the
 549 contrails. This behaviour is as expected and agrees with the position of clusters PW, YC2 and YC1
 550 on the expansion coefficient diagram (Fig. 2). Indeed, the decrease of the C_{j2} coefficient is
 551 associated to a side scattering enhancement. Therefore, very young contrails are composed mainly
 552 of spherical ice crystals for which the phase functions indicate a substantial scattering at forward
 553 angles and much lower scattering at sideward angles. As the contrails evolve, these features smooth
 554 out leading to phase functions with a featureless flat behaviour at side scattering angles. Finally, the

555 averaged normalized phase functions of aged contrails and polluted cirrus are similar to each other.
556 This also explains that they are difficult to discriminate within the PCA.

557 Figure 6c presents the extinction coefficient statistics. All the aged contrails (cluster AC1
558 and AC2) exhibit extinction coefficients lower than 2 km^{-1} . Also 80% of the sampled polluted cirrus
559 (cluster PC) show such low extinction coefficients. For younger contrails (cluster YC1 and YC2),
560 the extinction coefficients can reach 5 km^{-1} . Largest extinction coefficients are found in primary
561 wake measurements (cluster PW) with values up to 8 km^{-1} . Still, the main fraction (more than 50%
562 of data points) of young contrail data yields extinction coefficients from 0 to 1 km^{-1} .

563 Concentrations of chemical species can also be used to characterize contrail/cirrus
564 properties. The concentration depends strongly on the type of the tracked aircraft. Figure 6d shows
565 the mean concentration of nitrogen oxide NO for the six individual clusters. Young contrail NO
566 concentrations (cluster PW, YC1 and YC2) can reach values up to 10 nmol mol^{-1} (corresponding to
567 10% of measurements). For primary wake measurements (PW in black) a higher concentration can
568 be reached. Approximately 1% of the data have concentrations close to 60 nmol mol^{-1} in the
569 primary wake. In contrast, in aged contrails and in polluted cirrus (cluster AC1, AC2 and PC) NO
570 concentrations higher than 2 nmol mol^{-1} do not exceed 1% of cases. Indeed, after exhaust,
571 concentrations of nitrogen oxide NO and sulphur dioxide SO₂ created by combustion reactions
572 decrease rapidly due to the dispersion in the upper troposphere and reactions with other molecules.

573 Finally, Figure 6e shows the saturation conditions with respect to ice for all clusters. The
574 median ambient relative humidity of all clusters is near 95%. Cluster AC1 and PC (yellow and blue
575 lines respectively) exhibit median RHI values close to 110% and 120% respectively. These higher
576 values are suitable for the persistence of the contrail and the formation of cirrus clouds
577 Supersaturated conditions are not reached for the measurements gathered in the primary wake
578 cluster (PW). Low humidity values may well occur in primary wakes with non-persisting contrails.

579 These results highlight that the principal component analysis, based on the ASC
580 measurements described in Sect. 3, can be used to discriminate contrail phases. Specific optical and
581 chemical properties can thus be derived for each contrail phase and can be related to their evolution.

582 **4.2 Microphysical cluster properties**

583 Microphysical properties are assessed using the combination of FSSP-300 and 2DC
584 measurements. The data cover hydrometeor diameters ranging from $0.5 \text{ }\mu\text{m}$ to $800 \text{ }\mu\text{m}$, but with an
585 instrument gap in the size range from $17 \text{ }\mu\text{m}$ to $50 \text{ }\mu\text{m}$. Figure 7 shows the averaged number
586 particle size distributions (PSD) for each cluster and for all flights of the study (8 flights from
587 CONCERT-1 and 2). In the instrument gap of the PSD we use linear interpolation in logarithmic
588 space. Therefore, the derived microphysical properties are to be taken with caution.

589 PSD measurements in cirrus and contrails differ significantly depending on ambient air
 590 conditions, measurement methods (instrument limitation (Gayet et al., 2002), and air speed (Febvre
 591 et al., 2009)). Previous studies show that a 3-h old contrail cirrus with an effective diameter close to
 592 20 μm (Voigt et al., 2017) and number concentration larger than 0.1cm^{-3} (Schumann et al., 2017)
 593 can be composed of ice crystals with sizes up to 100 μm (blue dashed line, contrail cirrus figure 7).
 594 This differs from the PSD of the natural cirrus presented by Voigt et al. (2017) (dashed black line),
 595 which has an order of magnitude lower particle number concentration. In natural cirrus at mid-
 596 latitudes, ice crystals with size up to 1600 μm were observed during the ML-CIRRUS campaign
 597 (dark dashed line Figure 7, Voigt et al., 2017).

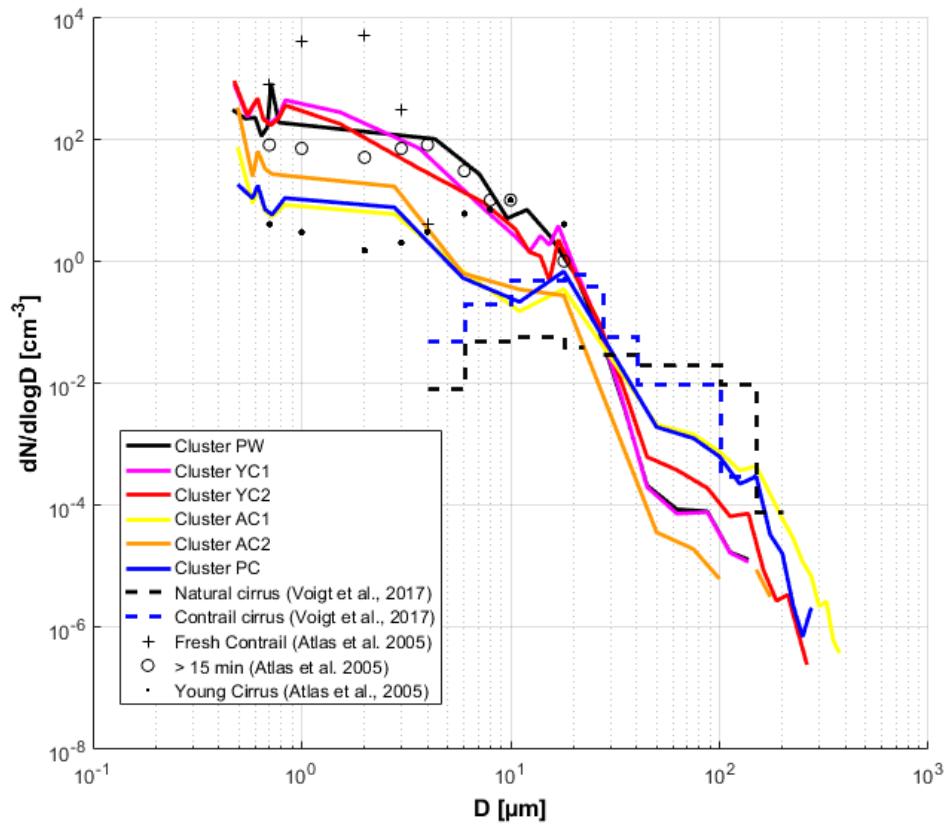


Figure 7: Number particle size distribution for each cluster including all data points of all flights. FSSP-300 measurements from 0.5 to 17 μm and 2DC measurements from 50 μm to 800 μm . The data are linearly interpolated in logarithm space in the gap between 17 μm and 50 μm .

598 Figure 7 shows that the mean number PSDs of each cluster are mainly consistent with the
 599 cluster definition and previous studies (Atlas et al., 2009; Voigt et al., 2017). Indeed, two categories
 600 of PSD can be observed. Within the FSSP-300 size range, PSD relative to old contrails (cluster
 601 AC1 and AC2) and polluted cirrus (cluster PC) exhibit number concentration of small ice particles
 602 one order of magnitude lower than young contrails (clusters YC1 and YC2) and primary wake
 603 (cluster PW). Differences in this size range may reflect uncertainties of the FSSP-300 number
 604 concentration measurements. The statistical uncertainty is close to 30% for typical concentrations of
 605 5cm^{-3} but can reach 75% for concentrations of approximately 0.5cm^{-3} (Gayet et al., 2002).
 606 However, we can still discriminate primary wake measurements (cluster PW) from secondary wake
 607 measurements (clusters YC1 and YC2) in the 3 to 10 μm size range. Differences observed between
 608 the PSD of PW/YC1/YC2 and AC1/AC2/PC can be explained by the production of small ice

609 crystals (from 1 to 10 μm) in fresh exhaust plumes followed by rapid dilution during subsequent
 610 minutes after the exhaust.

611 Higher concentrations of ice crystals with diameters larger than 100 μm are observed for
 612 polluted cirrus (cluster PC) and for well-developed contrails (cluster AC1). The average PSD of
 613 AC1 cluster shows much larger ice concentrations (around 10 times) compared to YC1 cluster
 614 within the 2DC size range.

615 It is important to note that shattering effects can significantly influence the PSD
 616 measurements especially when particles with diameters higher than 100 μm are present. Polluted
 617 cirrus or aged contrail measurements could be subject to such artefacts even though the
 618 concentrations of large ice particles were low in the aged contrails and in the polluted cirrus cases
 619 during these two campaigns. Shattering effects are likely to be small for the measurements in young
 620 contrails.

Extinction (km^{-1})		mean	std	Median	prctile 25	prctile 75
cluster	PW	4.230	3.820	3.308	1.104	6.485
	YC1	0.720	0.410	0.680	0.351	1.026
	YC2	2.070	2.655	1.017	0.271	2.836
	AC1	0.212 (0.204)	0.465 (0.456)	0.037 (0.033)	0.008 (0.005)	0.152 (0.138)
	AC2	0.114 (0.090)	0.163 (0.149)	0.060 (0.038)	0.007 (0.003)	0.135 (0.094)
	PC	0.207 (0.197)	0.363 (0.360)	0.072 (0.062)	0.032 (0.026)	0.178 (0.160)

IWC (mg m^{-3})		mean	std	Median	prctile 25	prctile 75
cluster	PW	8.173	10.586	5.573	1.665	11.363
	YC1	0.191	0.107	0.168	0.111	0.281
	YC2	4.860	8.918	1.235	0.218	6.604
	AC1	5.707 (5.705)	25.120 (25.120)	0.124 (0.122)	0.007 (0.004)	1.126 (1.123)
	AC2	0.310 (0.304)	1.103 (1.103)	0.112 (0.093)	0.005 (0.002)	0.290 (0.285)
	PC	3.024 (3.022)	8.845 (8.845)	0.218 (0.214)	0.080 (0.079)	0.641 (0.639)

NTOTAL (cm^{-3})		mean	std	Median	prctile 25	prctile 75
cluster	PW	172.965	114.497	152.398	95.564	223.374
	YC1	409.726	205.625	405.127	230.907	603.187
	YC2	188.139	199.736	125.344	52.584	236.100
	AC1	8.148 (0.372)	24.646 (2.103)	1.688 (0.086)	0.027 (0.027)	3.311 (0.179)
	AC2	29.517 (0.427)	44.723 (1.005)	8.021 (0.128)	0.0120 (0.020)	46.762 (0.290)
	PC	6.646 (0.360)	7.237 (0.864)	4.602 (0.213)	0.110 (0.110)	8.354 (0.394)

Table 3: Optical and microphysical properties for each cluster according interpolated particle size distributions from FSSP-300 and 2DC measurements. Values in parenthesis correspond to number concentrations for sizes larger than 3 μm .

621 Table 3 presents ice water content (IWC, in mg m^{-3}) and total number concentrations of ice
 622 crystals (NTOTAL, in cm^{-3}) derived from the measured PSD for each cluster. The extinction
 623 coefficient (in km^{-1}) obtained from the PN measurements is also displayed. The aged contrail
 624 clusters (AC1 and AC2) and the polluted cirrus cluster (PC) include some data points at
 625 temperatures higher than -38°C . These values cannot be contrails and are excluded from this
 626 analysis. Ice particles with diameters higher than 3 μm are considered for aged contrails and
 627 polluted cirrus to exclude possible contributions from large aerosol particles, as in the earlier studies
 628 of Krämer et al. (2009) and Voigt et al. (2017), and these values are shown in parenthesis. These
 629 results again show that each cluster can be related to a specific contrail phase, and their properties
 630 can be compared to previous studies.

631 In terms of cluster mean values, the microphysical and optical properties of cluster PW
632 agree with the cloud properties expected in the primary wakes. The extinction coefficient has a
633 mean value of 4.23 km^{-1} , IWC is close to 8 mg m^{-3} , and the number concentration yields a typical
634 value of $173 \text{ particles cm}^{-3}$. These properties are in agreement with previous measurement reported
635 by Gayet et al. (2012) with particle number concentrations close to 200 cm^{-3} for contrails less than
636 60 s after their formation. Their work also reports extinction coefficient around 7 km^{-1} presenting
637 the highest values of the contrail lifetime.

638 Young (clusters YC1 and YC2) and aged contrails (clusters AC1 and AC2) exhibit
639 distinctive differences in their extinction coefficients and their concentrations of ice particles.
640 Compared to aged contrails, young contrails have higher extinction coefficients and ice number
641 concentrations, with values larger than 0.7 km^{-1} and 170 cm^{-3} , respectively. Indeed, the averaged
642 extinction and number concentration values of aged contrails do not exceed 0.4 km^{-1} and 30 cm^{-3}
643 (0.5 cm^{-3} for diameters higher than $3 \mu\text{m}$), respectively. The ice number concentrations are in
644 agreement with previous results with values between 200 and 100 cm^{-3} for contrail ages between 60
645 s and 3 min, and around 5 cm^{-3} for contrail ages around 10 min (Goodman et al., 1998 ; Lawson et
646 al., 1998 ; Schröder et al., 2000 ; Schäuble et al., 2009 ; Gayet et al., 2012 ; Voigt et al., 2017). For
647 aged contrails, concentrations of ice particles with sizes greater than $3 \mu\text{m}$ are below 0.5 cm^{-3} ,
648 which agree with concentrations presented in other contrail studies (close to 1 cm^{-3} in Lawson et al.,
649 1998 and Schumann et al., 2017). Also aged contrails IWC and extinction coefficients mean values
650 lie between 0.3 mg m^{-3} and 5.7 mg m^{-3} and 0.09 and 0.2 km^{-1} , respectively. These values are only
651 weakly sensitive to the used cut-off size (below or above $3 \mu\text{m}$) and are in accordance with previous
652 studies where IWC values up to 10 mg m^{-3} and extinction coefficient below 0.5 km^{-1} were measured
653 (Schröder et al., 2000; Febvre et al., 2009; De Leon et al., 2012).

654 Our results also show that differences greater than 5 m mg^{-3} can be found within young
655 contrails (YC1 and YC2) and aged contrails (AC1 and AC2) clusters. This variability could be
656 attributed to a small number of large particles with diameter higher than $20 \mu\text{m}$ in YC1 and AC2
657 compared to YC2 and AC1 clusters.

658 Polluted cirrus properties are analysed for ice particles with size larger than $3 \mu\text{m}$. The mean
659 ice particle concentration of $0.36 \pm 0.9 \text{ cm}^{-3}$ is in agreement with previous cirrus studies where
660 values are retrieved between 0.5 and 0.005 cm^{-3} (Heymsfield et al., 2017) and typical average value
661 of 0.1 cm^{-3} was found by Voigt et al. (2017). IWC and extinction coefficients values (3.02 mg m^{-3}
662 and 0.20 km^{-1} , respectively) are significantly higher than the value found in clean cirrus cases
663 (0.055 mg m^{-3} and 0.023 km^{-1} , Schumann et al., 2017; Atlas and Wang, 2010), but are more
664 consistent with median values reported from Krämer et al. (2016) and Heymsfield et al. (2017)
665 (1.85 mg m^{-3} for temperatures between -60 and -50°C). Optical and microphysical properties of the
666 polluted cirrus are closer to the ones obtained for aged contrails. As mentioned in section 4.1, cirrus
667 observed during CONCERT campaigns are largely influenced by high-density air traffic over
668 Germany and it is thus still difficult to separate aged-contrails from natural cirrus based on their
669 scattering properties.

670

671 **Conclusions**

672 In this study, a new form of statistical analysis of contrail to cirrus evolution is presented,
673 based on two intensive contrail measurement campaigns, CONCERT-1 and CONCERT-2. The data
674 are used to study optical and microphysical properties of contrails during their evolution from
675 young contrails to contrail-cirrus clouds. The combination of optical, microphysical, and chemical

676 airborne measurements with aircraft chasing information from ATC provides an extended view of
677 cloud properties.

678 A Principal Component Analysis (PCA) methodology was applied to the measured Polar
679 Nephelometer scattering phase function data to facilitate the discrimination of cloud properties in
680 different contrail phases. The PCA results were derived first for two reference flights that sampled
681 contrails and cirrus in various development stages, including the primary wake, the young
682 secondary wake, old contrails (few minutes after formation) and polluted cirrus. For these flights,
683 the PCA clearly demonstrates its potential to discriminate different groups of clouds, justifying the
684 use of these two flights as a benchmark. Thereafter, the scattering phase functions measured during
685 other CONCERT flights were projected into the space of principal components obtained from the
686 two reference flights. Individual data points were assigned to the predefined cluster with minimum
687 Mahalanobis distances. From the entire data set, the cloud properties in the various contrail
688 development stages can be analysed separately.

689 The analysis demonstrates that the clearest separation between clusters is derived from
690 particle shape, which impacts the scattering phase function and the derived asymmetry parameter
691 gPN. The asymmetry parameter clearly separates young contrails (gPN of 0.72 to 0.80) from
692 contrail/cirrus with gPN ranging from 0.80 to 0.88. Since the exact contrail age was not always
693 known, young and aged contrails are classified also by their optical and chemical properties. The
694 measured NO concentrations are also useful to distinguish cirrus from old contrails. However, no
695 strictly clean cirrus has been observed during these two campaigns due to strong influence from
696 dense air traffic over Germany.

697 Particle size spectra and mean ice particle number concentration, extinction and ice water
698 content have been also determined for each cluster. The various clusters clearly show different size
699 distributions. In good agreement with previous findings, we find that young contrails have more
700 than a factor of ten higher number concentrations of small ice crystals (with diameters lower than
701 20 μm) than aged contrails. On the other hand, aged contrails and polluted cirrus contain larger ice
702 crystals, with diameters larger than 75 μm . The optical and microphysical properties of the aged
703 contrails are often similar to those found in ambient cirrus which may be polluted cirrus. For
704 polluted cirrus, the agreement with previous cirrus data is better when considering only ice particles
705 with diameter higher than 3 μm . The results show that the PCA method allows to identify and
706 discriminate different contrail growth stages and to provide an independent method for the
707 characterization of the evolution of contrail properties.

708 In agreement with Shcherbakov et al. (2016), who characterised volcanic and cirrus using
709 optical measurements, the PCA method has been clearly shown here to be suitable for contrail
710 studies. The additional use of microphysical and chemical measurements can be added to the PCA
711 method in order to improve the selection of contrail phases. Different ranges of extinction or
712 asymmetric coefficients could be also used for PCA analyses in this perspective. However,
713 additional parameters should be carefully selected to limit the bias introduced by the limitations of
714 the probes and the optimal selection may vary from one measurement campaign to another.

715 Accurate modelling of cirrus or contrails' single scattering properties is required for the
716 interpretation of remote sensing measurements. Therefore, measurements of the optical
717 characteristics of ice crystals in natural conditions are still needed for validation of numerical
718 techniques and for the determination of free parameters in light scattering models. In this context,
719 the results from the PCA could be used to develop representative parameterizations of the scattering
720 properties and the ice crystals' shapes and sizes observed in the visible wavelength range.

721 **Acknowledgments**

722 We thank for financial support by the Helmholtz Association under contract VH-NG-309 and
723 W2/W3-60. Part of this work was funded by DFG SPP HALO 1294 contract VO1504/4-1, and by
724 the DLR project Eco2Fly in ML-CIRRUS-cirrus special issue. We thank Lufthansa, the DLR flight
725 department and the Deutsche Flugsicherung for excellent support during the campaign. The in-situ
726 data can be found in the HALO-database (<https://halo-db.pa.op.dlr.de/>).

727 **References**

728 Baran, A.J., Gayet, J.-F., and Shcherbakov, V.: On the interpretation of an unusual in-situ measured
729 ice crystal scattering phase function. *Atmospheric Chemistry and Physics* 12, 9355–9364, 2012.

730
731 Baumgardner, D., Dye, J.E., Gandrud, B.W., and Knollenberg, R.G.: Interpretation of
732 measurements made by the forward scattering spectrometer probe (FSSP-300) during the
733 Airborne Arctic Stratospheric Expedition. *Journal of Geophysical Research* 97, 8035–8046, 1992.

734
735 Borrmann, S., Luo, B., and Mishchenko, M.: Application of the T-Matrix Method to the
736 Measurement of Aspherical (Ellipsoidal) Particles with Forward Scattering Optical Particle
737 Counters. *Journal of Aerosol Science* 31, no. 7 (2000): 789–799, 2000.

738
739 Burkhardt, U., Kärcher, B., and Schumann, U.: Global modeling of the contrail and contrail cirrus
740 climate impact. *Bulletin of the American Meteorological Society* 91, 479–484, 2010.

741
742 Burkhardt, U. and Kärcher, B.: Global radiative forcing from contrail cirrus. *Nature Climate*
743 *Change*, 1(1), 54–58, 2011.

744
745 Carleton, A.M., Silva, A.D., Aghazarian, M.S., Bernhardt, J., Travis, D.J., and Allard, J.: Mid-
746 season climate diagnostics of jet contrail “outbreaks” and implications for eastern US sky-cover
747 trends. *Climate Research*, 56, 209–230, 2013.

748
749 Chen, C.-C. and Gettelman, A.: Simulated 2050 aviation radiative forcing from contrails and
750 aerosols. *Atmospheric Chemistry and Physics*, 16(11), 7317–7333, 2016.

751
752 Duda, D. P., Minnis, P., Khlopenkov, K., Chee, T.L., and Boeke, R.: Estimation of 2006 Northern
753 Hemisphere Contrail Coverage Using MODIS Data. *Geophysical Research Letters*, 40, 612-617,
754 doi:10.1002/grl.50097, 2013.

755
756 Febvre, G., Gayet, J.-F., Minikin, A., Schlager, H., Shcherbakov, V., Jourdan, O., Busen, R., Fiebig,
757 M., Kärcher, B., and Schumann, U.: On optical and microphysical characteristics of contrails and
758 cirrus. *Journal of Geophysical Research: Atmospheres* (1984–2012) 114, 2009.

759
760 Frömming, C., Ponater, M., Dahlmann, K., Grewe, V., Lee, D.S., and Sausen, R.: Aviation-induced
761 radiative forcing and surface temperature change in dependency of the emission altitude. *Journal*
762 *of Geophysical Research: Atmospheres* (1984–2012) 117, 2012.

763
764 Gayet, J.F., Crépel, O., Fournol, J.F., and Oshchepkov, S.: A new airborne Polar Nephelometer for
765 the measurements of optical and microphysical cloud properties. Part I: Theoretical design. In
766 *Annales Geophysicae*, pp. 451–459, 1997.

767

768 Gayet, J.-F., Auriol, F., Minikin, A., Ström, J., Seifert, M., Krejci, R., Petzold, A., Febvre, G., and
769 Schumann, U.: Quantitative Measurement of the Microphysical and Optical Properties of Cirrus
770 Clouds with Four Different in Situ Probes: Evidence of Small Ice Crystals. *Geophysical Research*
771 *Letters* 29, no. 24: 2230. doi:10.1029/2001GL014342, 2002.
772

773 Gayet, J.-F., Ovarlez J., Shcherbakov, V., Ström, J., Schumann, U., Minikin, A., Auriol, F., Petzold,
774 A., and Monier M.: Cirrus Cloud Microphysical and Optical Properties at Southern and Northern
775 Midlatitudes during the INCA Experiment. *Journal of Geophysical Research: Atmospheres* 109,
776 no. D20 : D20206. doi:10.1029/2004JD004803, 2004.
777

778 Gayet, J.-F., Shcherbakov, V., Voigt, C., Schumann, U., Schäuble, D., Jeßberger, P., Petzold, A.,
779 Minikin, A., Schlager, H., Dubovik, O., and Lapyonok, T.: The evolution of microphysical and
780 optical properties of an A380 contrail in the vortex phase. *Atmospheric Chemistry and Physics*.
781 12, 6629–6643, 2012.
782

783 Garrett, T.J., Gerber, H., Baumgardner, D.G., Twohy, C.H., and Weinstock, E.M.: Small, highly
784 reflective ice crystals in low-latitude cirrus. *Geophysical Research Letters* 30, 2132, 2003.
785

786 Gettelman, A., and Chen, C.: The climate impact of aviation aerosols. *Geophysical Research*
787 *Letters*, 40, 2785–2789, doi:10.1002/grl.50520, 2013.
788

789 Gierens, K. and Dilger, F.: A climatology of formation conditions for aerodynamic contrails,
790 *Atmospheric Chemistry and Physics*, 13, 10847-10857, doi:10.5194/acp-13-10847-2013, 2013.
791

792 Graf, K., Schumann, U., Mannstein, H., and Mayer, B.: Aviation induced diurnal North Atlantic
793 cirrus cover cycle. *Geophysical Research Letters* 39, L16804, doi:10.1029/2012GL052590, 2012.
794

795 Goodman, J., Pueschel, R.F., Jensen, E.J., Verma, S., Ferry, G.V., Howard, S.D., Kinne, S.A., and
796 Baumgardner, D.: Shape and size of contrails ice particles. *Geophysical Research Letters* 25,
797 1327–1330, 1998.
798

799 Heller, R., Voigt, C., Beaton, S., Dörnbrack, A., Kaufmann, S., Schlager, H., Wagner, J., Young,
800 K., and Rapp, M.: Mountain waves modulate the water vapor distribution in the UTLS,
801 *Atmospheric Chemistry and Physics*, doi:10.5194/acp-2017-334, *Atmos. Chem. Phys.*, 2017.
802

803 Heymsfield, A.J., and Parrish, J.L.: A computational technique for increasing the effective sampling
804 volume of the PMS two-dimensional particle size spectrometer. *Journal of Applied Meteorology*
805 17, 1566–1572, 1978.
806

807 Heymsfield, A., Baumgardner, D., DeMott, P., Forster, P., Gierens, K., and Kärcher, B.: Contrail
808 Microphysics. *Bulletin of the American Meteorological Society* 91, 465–472, 2010.
809

810 Heymsfield, A. J., Krämer, M., Luebke, A., Brown, P., Cziczko, D. J., Franklin, C., Lawson, P.,
811 Lohmann, U., McFarquhar, G., Ulanowski, Z. and Van Tricht, K.: Cirrus Clouds, *Meteorological*
812 *Monographs*, 58, 2.1-2.26, doi:10.1175/AMSMONOGRAPHS-D-16-0010.1, 2017.
813

814 Irvine, E.A., Hoskins, B.J., and Shine, K.P.: The dependence of contrail formation on the weather
815 pattern and altitude in the North Atlantic. *Geophysical Research Letters* 39, L12802,
816 doi:10.1029/2012GL051909, 2012.
817

818 Järvinen, E., Schnaiter, M., Mioche, G., Jourdan, O., Shcherbakov, V.N., Costa, A., Afchine, A.,
819 Krämer, M., Heidelberg, F., Jurkat, T., Voigt, C., Schlager, H., Nichman, L., Gallagher, M.,
820 Hirst, E., Schmitt, C., Bansemer, A., Heymsfield, A., Lawson, P., Tricoli, U., Pfeilsticker, K.,
821 Vochezer, P., Möhler, O., and Leisner, T.: Quasi-spherical Ice in Convective Clouds, *Journal of*
822 *Atmospheric Sciences*, doi:10.1175/JAS-D-15-0365.1, 2016.

823

824 Jansen, J. and Heymsfield, A. J.: Microphysics of aerodynamic contrail formation processes,
825 *Journal of Atmospheric Sciences*, 72(9), 3293–3308, 2015.

826

827 Jeßberger, P., Voigt, C., Schumann, U., Sölch, I., Schlager, H., Kaufmann, S., Petzold, A.,
828 Schäuble, D., and Gayet, J.F.: Aircraft type influence on contrail properties, *Atmospheric*
829 *Chemistry and Physics*, 13, 11965-11984, doi:10.5194/acp-13-11965-2013, 2013.

830

831 Jourdan, O., Oshchepkov, S., Gayet, J.-F., Shcherbakov, V., and Isaka, H.: Statistical analysis of
832 cloud light scattering and microphysical properties obtained from airborne measurements. *Journal*
833 *of Geophysical Research* 108, 4155, 2003.

834

835 Jourdan, O., Mioche, G., Garrett, T.J., Schwarzenböck, A., Vidot, J., Xie, Y., Shcherbakov, V.,
836 Yang, P., and Gayet, J.-F.: Coupling of the microphysical and optical properties of an Arctic
837 nimbostratus cloud during the ASTAR 2004 experiment: Implications for light-scattering
838 modeling. *Journal of Geophysical Research: Atmospheres* (1984–2012) 115, 2010.

839

840 Jurkat, T., Voigt, C., Arnold, F., Schlager, H., Aufmhoff, H., Schmale, J., Schneider, J.,
841 Lichtenstern, M., and Dörnbrack, A.: Airborne stratospheric ITCIMS-measurements of SO₂, HCl,
842 and HNO₃ in the aged plume of volcano Kasatochi, *Journal of Geophysical Research*, 115,
843 D00L17, doi:10.1029/2010JD013890, 2010.

844

845 Jurkat, T., Voigt, C., Arnold, F., Schlager, H., Kleffmann, J., Aufmhoff, H., Schäuble, D., Schäfer,
846 M., and Schumann, U.: Measurements of HONO, NO, NO_y and SO₂ in aircraft exhaust plumes
847 at cruise, *Geophysical Research Letters*, 38, L10807, doi:10.1029/2011GL046884, 2011.

848

849 Jurkat, T., Kaufmann, S., Voigt, C., Schäuble, D., Jeßberger, P., and Ziereis, H.: The airborne mass
850 spectrometer AIMS – Part 2: Measurements of trace gases with stratospheric or tropospheric
851 origin in the UTLS, *Atmospheric Measurement Technics*, 9, 1907–1923, doi:10.5194/amt-9-
852 1907-2016, 2016.

853

854 Kärcher, B., and Voigt, C.: Formation of nitric acid/water ice particles in cirrus clouds, *Geophysical*
855 *Research Letters*, 33, L08806, doi:10.1029/2006GL025927, 2006.

856

857 Kärcher, B., and Voigt, C.: Susceptibility of contrail ice crystal numbers to aircraft soot particle
858 emissions, *Geophysical Research Letters*, 44, 8037-8046, doi:10.1002/2017GL074949, 2017.

859

860 Kärcher, B., and Yu, F.: Role of aircraft soot emissions in contrail formation. *Geophysical Research*
861 *Letters*, 36, L01804, doi:10.1029/2008GL036649, 2009.

862

863 Kaufmann, S., Voigt, C., Jeßberger, P., Jurkat, T., Schlager, H., Schwarzenboeck, A., Klingebiel,
864 M., and Thornberry, T.: In situ measurements of ice saturation in young contrails, *Geophysical*
865 *Research Letters*, 41, doi:10.1002/2013GL058276, 2014.

866

867 Kaufmann, S., Voigt, C., Jurkat, T., Thornberry, T., Fahey, D. W., Gao, R.-S., Schlage, R.,
868 Schäuble, D., and Zöger, M.: The airborne mass spectrometer AIMS – Part 1: AIMS-H₂O for
869 UTLS water vapor measurements, *Atmospheric Measurement Technics*, 9, 939-953,
870 doi:10.5194/amt-9-939-2016, 2016.

871

872 Krämer, M., Schiller, C., Afchine, A., Bauer, R., Gensch, I., Mangold, A., Schlicht, S., Spelten, N.,
873 Sitnikov, N. and Borrmann, S.: Ice supersaturations and cirrus cloud crystal numbers,
874 *Atmospheric Chemistry and Physics*, 9(11), 3505–3522, 2009.

875

876 Krämer, M., Rolf, C., Luebke, A., Afchine, A., Spelten, N., Costa, A., Meyer, J., Zöger, M., Smith,
877 J., Herman, R. L., Buchholz, B., Ebert, V., Baumgardner, D., Borrmann, S., Klingebiel, M., and
878 Avallone, L.: A microphysics guide to cirrus clouds – Part 1: Cirrus types, *Atmos. Chem. Phys.*,
879 16, 3463-3483, <https://doi.org/10.5194/acp-16-3463-2016>, 2016

880

881 Kübbeler, M., Hildebrandt, M., Meyer, J., Schiller, C., Hamburger, Th., Jurkat, T., Minikin, A.,
882 Petzold, A., Rautenhaus, M., Schlager, H., Schumann, U., Voigt, C., Spichtinger, P., Gayet, J.-F.,
883 Gourbeyre, C., and Krämer, M.: Thin and subvisible cirrus and contrails in a subsaturated
884 environment, *Atmospheric Chemistry and Physics*, 11, 5853-5865, doi:10.5194/acp-11-5853-
885 2011, 2011.

886

887 Lawson, R. Paul, Andrew J. Heymsfield, Steven M. Aulenbach, et Tara L. Jensen. « Shapes, sizes
888 and light scattering properties of ice crystals in cirrus and a persistent contrail during SUCCESS
889 ». *Geophysical research letters* 25, no 9: 1331–1334, 1998.

890

891 Lawson, R.P., O'Connor, D., Zmarzly, P., Weaver, K., Baker, B., Mo, Q., and Jonsson, H.: The 2D-
892 S (stereo) probe: Design and preliminary tests of a new airborne, high-speed, high-resolution
893 particle imaging probe. *Journal of Atmospheric and Oceanic Technology* 23, 1462–1477, 2006.

894

895 Lee, D.S., Pitari, G., Grewe, V., Gierens, K., Penner, J.E., Petzold, A., Prather, M.J., Schumann, U.,
896 Bais, A., and Berntsen, T.: Transport impacts on atmosphere and climate: Aviation. *Atmospheric
897 Environment* 44, 4678–4734, 2010.

898

899 Legendre, P., and Legendre, L.: *Numerical Ecology*, 2nd English ed., 853 pp., Elsevier Science,
900 New York, 1998.

901

902 De León, R.R., Krämer, M., Lee, D.S., and Thelen, J.C.: Sensitivity of radiative properties of
903 persistent contrails to the ice water path. *Atmospheric Chemistry and Physics*. 12, 7893–7901,
904 2012.

905

906 Lewellen, D.C.: Analytic solutions for evolving size distributions of spherical crystals or droplets
907 undergoing diffusional growth in different regimes. *Journal of the Atmospheric Sciences* 69,
908 417–434, 2012.

909

910 Lewellen, D.C., and Lewellen, W.S.: The effects of aircraft wake dynamics on contrail
911 development. *Journal of the Atmospheric Sciences* 58, 390–406, 2001.

912

913 Liou, K.N., Takano, Y., Yue, Q., and Yang, P.: On the radiative forcing of contrail cirrus
914 contaminated by black carbon. *Geophysical Research Letters*, 40, 778–784,
915 doi:10.1002/grl.50110, 2013.

916

917 De Maesschalck, R., Jouan-Rimbaud, D., and Massart, D.L.: The Mahalanobis Distance.
 918 Chemometrics and Intelligent Laboratory Systems 50, no. 1: 1–18. doi:10.1016/S0169-
 919 7439(99)00047-7, 2010.
 920

921 Meyer, J., Rolf, C., Schiller, C., Rohs, S., Spelten, N., Afchine, A., Zöger, M., Sitnikov, N.,
 922 Thornberry, T. D., Rollins, A. W., Bozóki, Z., Tátrai, D., Ebert, V., Kühnreich, B., Mackrodt, P.,
 923 Möhler, O., Saathoff, H., Rosenlof, K. H., and Krämer, M.: Two decades of water vapor
 924 measurements with the FISH fluorescence hygrometer: a review, Atmospheric Chemistry and
 925 Physics, 15, 8521–8538, doi:10.5194/acp-15-8521-2015, 2015.
 926

927 Mishchenko, M.I., Travis, L.D., Kahn, R.A., and West, R.A.: Modeling phase functions for dustlike
 928 tropospheric aerosols using a shape mixture of randomly oriented polydisperse spheroids. Journal
 929 of Geophysical Research 102, 16831–16, 1997.
 930

931 Moore, R. H., Thornhill, K. L., Weinzierl, B., Sauer, D., D’Ascoli, E., Kim, J., Lichtenstern, M.,
 932 Scheibe, M., Beaton, B., Beyersdorf, A. J., Barrick, J., Bulzan, D., Corr, C. A., Crosbie, E.,
 933 Jurkat, T., Martin, R., Riddick, D., Shook, M., Slover, G., Voigt, C., White, R., Winstead, E.,
 934 Yasky, R., Ziemba, L. D., Brown, A., Schlager, H., and Anderson, B. E.: Biofuel blending
 935 reduces particle emissions from aircraft engines at cruise conditions, Nature, 543, 411-415,
 936 10.1038/nature21420, 2017.
 937

938 Schäuble, D., Voigt, C., Kärcher, B., Stock, P., Schlager, H., Krämer, M., Schiller, C., Bauer, R.,
 939 Spelten, N., De Reus, M., Szakáll, M., Borrmann, S., Weers, U., and Peter T.: Airborne
 940 measurements of the nitric acid partitioning in persistent contrails, Atmospheric Chemistry and
 941 Physics, 9, 8189-8197, 2009.
 942

943 Schlager, H., Konopka, P., Schulte, P., Schumann, U., Ziereis, H., Arnold, F., Klemm, M., Hagen,
 944 D.E., Whitefield, P.D., and Ovarlez, J.: In situ observations of air traffic emission signatures in
 945 the North Atlantic flight corridor. Journal of Geophysical Research 102, 10739–10, 1997.
 946

947 Schröder, F., Kärcher, B., Durore, C., Ström, J., Petzold, A., Gayet, J.-F., Strauss, B., Wendling,
 948 P., and Borrmann, S.: On the Transition of Contrails into Cirrus Clouds. Journal of the
 949 Atmospheric Sciences 57, 464–480, 2000.
 950

951 Schumann, U.: On conditions for contrail formation from aircraft exhausts. Meteorologische
 952 Zeitschrift, 5, 4–23, 1996.
 953

954 Schumann, U., and Heymsfield, A.: On the lifecycle of individual contrails and contrail cirrus,
 955 Meteorological Monographs, 58, 3.1-3.24, doi: 10.1175/AMSMONOGRAPHS-D-16-0005.1,
 956 2017.
 957

958 Schumann, U., Jeßberger, P., and Voigt, C.: Contrail ice particles in aircraft wakes and their
 959 climatic importance, Geophysical Research Letters, 40, 2867-2872, doi: 10.1002/grl.50539, 2013.
 960

961 Schumann, U., Mayer, B., Gierens, K., Unterstrasser, S., Jessberger, P., Petzold, A., Voigt, C., and
 962 Gayet, J.-F.: Effective Radius of Ice Particles in Cirrus and Contrails. Journal of the Atmospheric
 963 Sciences, 68, 300–321, 2011.
 964

- 965 Schumann, U., Penner, J.E., Chen, Y., Zhou, C., and Graf, K.: Dehydration effects from contrails in
966 a coupled contrail-climate model, *Atmospheric Chemistry and Physics*, 15, 11179-11199, doi:
967 10.5194/acp-15-11179-2015, 2015.
968
- 969 Schumann, U., Kiemle, C., Schlager, H., Weigel, R., Borrmann, S., D'Amato, F., Krämer, M.,
970 Matthey, R., Protat, A., Voigt, C., and Volk, C. M.: Long-lived contrails and convective cirrus
971 above the tropical tropopause, *Atmospheric Chemistry and Physics*, 17, 2311-2346,
972 doi:10.5194/acp-17-2311-2017, 2017a.
973
- 974 Schumann, U., Baumann, R., Baumgardner, D., Bedka, S. T., Duda, D. P., Freudenthaler, V.,
975 Gayet, J.-F., Heymsfield, A. J., Minnis, P., Quante, M., Raschke, E., Schlager, H., Vázquez-
976 Navarro, M., Voigt, C. and Wang, Z.: Properties of individual contrails: a compilation of
977 observations and some comparisons, *Atmospheric Chemistry and Physics*, 17(1), 403–438,
978 doi:10.5194/acp-17-403-2017, 2017b.
979
- 980 Seber, G. A. F.: Multivariate analysis of variance and covariance. *Multivariate observations*, 433–
981 495, 1984.
982
- 983 Shcherbakov, V., Jourdan, O., Voigt, C., Gayet, J.F., Chauvigne, A., Schwarzenboeck, A., Minikin,
984 A., Klingebiel, M., Weigel, R., Borrmann, S., Jurkat, T., Kaufmann, S., Schlage, R., Gourbeyre,
985 C., Febvre, G., Lapyonok, T., Frey, W., Molleker, S., and Weinzierl, B.: Porous Aerosol in
986 Degassing Plumes of Mt. Etna and Mt. Stromboli. *Atmospheric Chemistry Physics* 16, no. 18:
987 11883–97. doi:10.5194/acp-16-11883-2016, 2016.
988
- 989 Spath, Helmuth. *The Cluster Dissection and Analysis Theory FORTRAN Programs Examples*.
990 Prentice-Hall, Inc., 1985.
991
- 992 Sussmann, R., and Gierens, K.M.: Lidar and numerical studies on the different evolution of vortex
993 pair and secondary wake in young contrails. *Journal of Geophysical Research: Atmospheres* 104,
994 2131–2142, 1999.
995
- 996 Sussmann, R., and Gierens, K.M.: Differences in early contrail evolution of two-engine versus four-
997 engine aircraft: Lidar measurements and numerical simulations. *Journal of Geophysical*
998 *Research: Atmospheres* 106, 4899–4911, 2001.
999
- 1000 Vazquez-Navarro, M., Mannstein, H. and Kox, S.: Contrail life cycle and properties from 1 year of
1001 MSG/SEVIRI rapid-scan images, *Atmospheric Chemistry and Physics*, 15(15), 8739–8749, 2015.
1002
- 1003 Voigt C., Schlager, H., Ziereis, H., Kärcher, B., Luo, B.P., Schiller, C., Krämer, M., Popp, P.J., Irie,
1004 H., and Kondo, Y.: Nitric acid in cirrus clouds, *Geophysical Research Letters*, 33, L05803,
1005 doi:10.1029/2005GL025159, 2006.
1006
- 1007 Voigt, C., Schumann, U., Jurkat, T., Schäuble, D., Schlager, H., Petzold, A., Gayet, J.-F., Krämer,
1008 M., Schneider, J., Borrmann, S., Schmale, J., Jessberger, P., Hamburger, T., Lichtenstern, M.,
1009 Scheibe, M., Gourbeyre, C., Meyer, J., Kübbeler, M., Frey, W., Kalesse, H., Butler, T.,
1010 Lawrence, M.G., Holzäpfel, F., Arnold, F., Wendisch, M., Döpelheuer, A., Gottschaldt, K.,
1011 Baumann, R., Zöger, M., Sölch, I., Rautenhaus, M., and Dörnbrack, A.: In-situ observations of
1012 young contrails - Overview and selected case studies from the CONCERT campaign,
1013 *Atmospheric Chemistry and Physics*, 10, 9039–9056, doi:10.5194/acp-10-9039-2010, 2010.
1014

1015 Voigt, C., Schumann, U., Jessberger, P., Jurkat, T., Petzold, A., Gayet, J.-F., Krämer, M.,
1016 Thornberry, T., and Fahey, D.: Extinction and optical depth of contrails, *Geophysical Research*
1017 *Letters*, 38, L11806, doi:10.1029/2011GL04718, 2011.

1018

1019 Voigt, C., Jessberger, P., Jurkat, T., Kaufmann, S., Baumann, R., Schlager, H., Bobrowski, N.,
1020 Giuffrida, G., and Salerno, G.: Evolution of CO₂, SO₂, HCl, and HNO₃ in the Volcanic Plumes
1021 from Etna. *Geophysical Research Letters*, 41, 6, 2196-2203. doi:10.1002/2013GL058974, 2014.

1022

1023 Voigt, C., Schumann, U., Minikin, A., Abdelmonem, A., Afchine, A., Borrmann, S., Boettcher, M.,
1024 Buchholz, B., Bugliaro, L., Costa, A., Curtius, J., Dollner, M., Dörnbrack, A., Dreiling, V., Ebert,
1025 V., Ehrlich, A., Fix, A., Forster, L., Frank, F., Fütterer, D., Giez, A., Graf, K., Groß, J.-U., Groß,
1026 S., Heimerl, K., Heinold, B., Hüneke, T., Järvinen, E., Jurkat, T., Kaufmann, S., Kenntner, M.,
1027 Klingebiel, M., Klimach, T., Kohl, R., Krämer, M., Krisna, T. C., Luebke, A., Mayer, B., Mertes,
1028 S., Molleker, S., Petzold, A., Pfeilsticker, K., Port, M., Rapp, M., Reutter, P., Rolf, C., Rose, D.,
1029 Sauer, D., Schäfler, A., Schlage, R., Schnaiter, M., Schneider, J., Spelten, N., Spichtinger, P.,
1030 Stock, P., Walser, A., Weigel, R., Weinzierl, B., Wendisch, M., Werner, F., Wernli, H., Wirth,
1031 M., Zahn, A., Ziereis, H., and Zöger, M.: ML-CIRRUS - The airborne experiment on natural
1032 cirrus and contrail cirrus with the high-altitude long-range research aircraft HALO, *Bulletin of*
1033 *the American Meteorological Society*, doi: 10.1175/BAMS-D-15-00213, 2017.

1034

1035 Xie, Y., Yang, P., Gao, B.-C., Kattawar, G.W., and Mishchenko, M.I.: Effect of ice crystal shape
1036 and effective size on snow bidirectional reflectance. *Journal of Quantitative Spectroscopy and*
1037 *Radiative Transfer* 100, 457–469, 2006.

1038

1039 Xie, Y., Yang, P., Kattawar, G.W., Minnis, P., and Hu, Y.X.: Effect of the inhomogeneity of ice
1040 crystals on retrieving ice cloud optical thickness and effective particle size. *Journal of*
1041 *Geophysical Research: Atmospheres* (1984–2012) 114, 2009.

1042

1043 Yang, P., Hong, G., Dessler, A.E., Ou, S.S., Liou, K.-N., and Minnis, P.: Contrails and induced
1044 cirrus: Optics and radiation. *Bulletin of the American Meteorological Society* 91, 473–478, 2010.

1045

1046 Ziereis, H., Schlager, H., Schulte, P., Velthoven, P. van, and Slemr, F.: Distributions of NO, NO_x,
1047 and NO_y in the upper troposphere and lower stratosphere between 28 and 61 N during
1048 POLINAT 2. *Journal of Geophysical Research: Atmospheres* (1984–2012) 105, 3653–3664,
1049 2000.

1050

1051 Zöger, M., Afchine, A., Eicke, N., Gerhards, M.-T., Klein, E., McKenna, D.S., Mörschel, U.,
1052 Schmidt, U., Tan, V., Tuitjer, F., Woyke, T., and Schiller, C. : Fast in situ stratospheric
1053 hygrometers: A new family of balloon-borne and airborne Lyman alpha photofragment
1054 fluorescence hygrometers. *Journal of Geophysical Research: Atmospheres*, 104, 1807-1816,
1055 1999.

1056